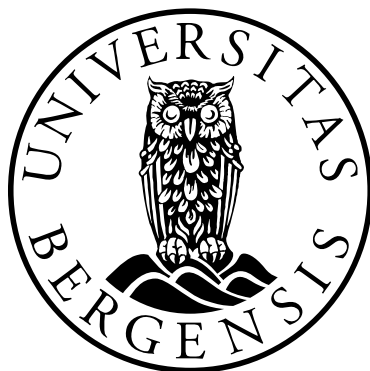


Small-scale turbulence dynamics under sea surface gravity waves

Mostafa Bakhoday Paskyabi



Dissertation for the degree philosophiae doctor (PhD)
at the University of Bergen

2014

Dissertation date: 20 August 2014

Scientific environment

This PhD study has been carried out at the Geophysical Institute (GFI), University of Bergen, funded by the Norwegian Center for Offshore Wind Energy (NORCOWE). The goals of this thesis have been aligned with the important vision of NORCOWE for exploitation of offshore wind energy as a natural sustainable, innovative, and cost efficient energy resource. This work describes the collection and interpretation of high quality oceanographic data sets relevant for offshore wind energy applications. The data were acquired during four field campaigns using the research vessels R/V Johan Hjort and R/V Håkon Mosby, operated by the Institute of Marine Research (IMR). A number of scientific collaborations were also established during the investigations with: the Norwegian Meteorological Institute (met.no); Swinburne University, Melbourne, Australia; the Applied Physics Laboratory (APL), Seattle, Washington, USA; and the candidate also participated in scientific meetings at the Oceanography Division of the Scripps Institution of Oceanography in San Diego, California, USA.

Acknowledgements

Writing this part has given me the chance to look back over the past four years' journey and remember not only the friends and family along the way, but also those who briefly crossed my path. Invaluable impressions have been left in my mind and heart, and here is where I wish to express my gratitude to those whom have made a difference in the features of this road.

Foremost, thanks to my supervisor, Prof. Ilker Fer, for his motivating guidance, advice, and endless patience. His inspiration and dedication to the work has motivated me in finding my own way, in developing and honing my skills, and in shaping the direction of my scientific future. I would like to express my heartfelt gratitude for all his contributions and the thoughtful, detailed comments on most all aspects of my thesis. It has greatly aided me in successfully completing my PhD, and in doing so within the allocated time.

To my co-advisor, Dr. Alastair D. Jenkins, thank you for the encouraging, insightful discussions and constructive feedbacks throughout these four years. Alastair, you have provided me with a rich basis from which to study and explore new ideas in my research. For this, I owe you special gratitude. I would also like to thank Prof. Joachim Reuder who has been extremely supportive in providing me with numerous opportunities to participate in both national and international activities. Joachim, you have left an indelible mark on my scientific growth for which I am very grateful. As PhD student at the Geophysical Institute, I have been surrounded by great colleagues, among whom Martin Flügge deserves special mention. Martin, you have not only been an incredible collaborator and co-worker, but also a wonderful friend. Thanks for the rich, happy, fruitful, and creative environment you have provided.

To the staff, researchers, and students at Swinburne University of Technology, Melbourne, Australia, I am grateful for the opportunity I had to visit and be a part of your group. Alex Babanin, Stefan Zieger, Malek Ghantous thank you for welcoming me as a friend and helping in the development of ideas in this thesis. To Ramsey Harcourt and Erik A. D'Asaro, Jim Thomson, Jun-Hong Liang, and Michael Schwendeman at Applied Physic Laboratory and Peter P. Sullivan (MMM Division, NCAR, Boulder, USA), thank you all for welcoming me during my visit. Many ideas originated from our productive exchanges. Ramsey, thanks for hosting me and for many fruitful discussions while at APL. Gratitude is due to Dr. James B. Edson from the University of Connecticut, USA, for providing me with an extensive data set and to Scott D. Miller for kindly providing me with some codes. Thank you Johannes Gemmrich for constructive comments on image processing during the Ocean Science Meeting. I also want to express my gratitude to Ken Melville, Luc lenain, and Grant Deane for the helpful discussions during my visit to the Scripps Institute, San Diego, USA.

Life in Bergen has been most enjoyable and exciting during the course of my PhD.

This is in no small measure due to role of many friends, a complete list of which it would be impossible to provide. However, Ali (Sarhadi), Roohollah, Iman, Mahbobeh, Mahdi, Zahra, Mohammad, Hamed, Sepideh, Atabak, Martin, Johannes, and Susana: thank you guys for ensuring I had a wonderful time outside of the academic environment To my officemates Basang and Pierre at the GFI, thank you. Furthermore, to the many anonymous reviewers at the various journals and conferences thank you for your constructive help and comments. I would also further like to thank the staff and students at GFI.

My dear parents, Sorayya and Ahmad, I have been able to achieve this degree, indeed all academic success thus far, because you instilled within me a love of science and a yearning after understanding. Thank you. Most importantly, my dear lovely lady Maryam, thank you with all of my heart. This thesis would not have been possible without your never-ending love, friendship, encouraging support and tireless enthusiasm during our (almost) seven years of marriage. Maryam, this achievement is the product of your love and endless light of hope, thank you.

And last, but not least, to those who have lent a hand during my PhD and I have failed to mention, my gratitude.

Abstract

The ocean surface is a complex boundary where air-sea fluxes of mass, momentum and energy take place. The processes at this dynamic interface are of great importance in the coupled atmosphere-ocean system. The coupling between winds, surface gravity waves, and currents in the adjacent turbulent boundary layers plays a significant role in the the global energy budget, and hence on synoptic weather system and the global climate. However, the characteristics of upper ocean turbulence very close to the air-sea interface still remain insufficiently resolved both theoretically and experimentally. This dissertation aims to improve the gap in our knowledge about air-sea interaction by combining theory, numerical model predictions, and high quality observations under various sea states and wind conditions.

An autonomous Microstructure Ocean Turbulence System (MATS) has been designed and constructed in collaboration with Rockland Scientific International, Canada, to collect long time series of turbulent quantities at a fixed level below the wavy air-sea interface. The system allows for measurements of the turbulent dissipation rate using shear probe signals. The motion of the platform is monitored using an inertial measurement unit. Four successful deployments have been carried out, including two periods with storm conditions in late 2011 and early 2012, respectively. Surface gravity waves were also estimated using a high-resolution pressure sensor mounted on the MATS. In addition, a direct covariance flux system was mounted on a moored buoy, and measurements of turbulent heat and momentum fluxes were performed approximately 3.7 m above the sea surface during a field campaign at Martha's Vineyard Coastal Observatory (MVCO), Massachusetts.

This dissertation also aims to improve the parameterizations in numerical modelling studies of upper ocean mixing, by incorporating the effects of wave forcing which are quantified by means of model-observation comparisons. Responsible mechanisms such as breaking and non-breaking waves, and Langmuir Circulation contributions to the enhanced dissipation rate of Turbulent Kinetic Energy (TKE) in the upper ocean are studied theoretically and numerically. A wave toolbox to be incorporated in the General Ocean Turbulence Model (GOTM) has been developed to implement wave effects in an upper ocean vertical mixing model. Moreover, statistics of small scale turbulence below the air-sea interface are investigated under a variety of environmental conditions using model results compared with MATS-measured TKE dissipation rates. The wave-modified model results are further compared with some published empirical parameterizations of the dissipation rate, and some other data from the literature. All model-observation study results support the importance of wave forcing in modulating and modifying upper ocean dynamics and the turbulence structure near the sea surface.

Outline with list of papers

The aim of this thesis is to investigate the importance of surface gravity waves for vertical mixing, both observationally, theoretically, and numerically. The measurements have been made using a Microstructure Autonomous Ocean Turbulence System (MATS) under various atmospheric forcing and sea state conditions. A one-dimensional modified numerical model is developed to include such wave-induced mechanisms as wave breaking, Langmuir turbulence, and the generation of turbulence by non-breaking waves. The model results are compared with data collected from MATS shear probes.

This thesis consists of 6 chapters together with six papers and four appendices. Chapter 1 presents an overview of the main features of upper ocean mixing under the influence of wave forcing. Chapter 2 provides a general scientific background, and Chapter 3 contains approaches and methods covering various aspects of wave interaction with currents and turbulence. Chapter 4 contains a more thorough descriptions of the approaches and methods used in this study. A summary of all papers included in this thesis is given in Chapter 5, and a summary and suggestions for further work are provided in Chapter 6.

The six papers included in this dissertation are listed as follows:

- Paper I:** Mostafa Bakhoday Paskyabi, Ilker Fer, and Alastair D. Jenkins, *Surface gravity wave effects on the upper ocean boundary layer: modification of a one-dimensional vertical mixing model*, Cont. Shelf Res., **38**, 63–78, 2012.
- Paper II:** Ilker Fer and Mostafa Bakhoday Paskyabi, *Autonomous ocean turbulence measurements using shear probes on a moored instrument*, J. Atmos. Ocean. Tech., **31**, 474–490, 2014.
- Paper III:** Mostafa Bakhoday Paskyabi and Ilker Fer, *Turbulence measurements in shallow water from a subsurface moored moving platform*, Energ. Proced., **35**, 307–316, 2013.
- Paper IV:** Mostafa Bakhoday Paskyabi and Ilker Fer, *Turbulence structure in the upper ocean: a comparative study of observations and modeling*, Ocean Dyn., **38**, 63–78, 2014.
- Paper V:** Mostafa Bakhoday Paskyabi and Ilker Fer, *The influence of surface gravity waves on the injection of turbulence in the upper ocean*, Nonlin. Proc. Geophys., accepted for publication.
- Paper VI:** Mostafa Bakhoday Paskyabi, Martin Flügge, James B. Edson, and Joachim Reuder, *Wave-induced characteristics of atmospheric turbulence flux measurements*, Energ. Proced., **35**, 102–112, 2013.

Contents

Scientific environment	i
Acknowledgements	iii
Abstract	v
Outline with list of papers	vii
1 Introduction	1
2 Scientific background	9
2.1 Surface gravity waves and wind-wave interaction	10
2.2 Wave-current interaction	11
2.2.1 Vortex force (vertically resolved approach)	12
2.2.2 Radiation stress (vertically integrated approach)	13
2.2.3 Hybrid approaches	14
2.3 Wave-turbulence interaction	16
2.3.1 TKE budgets in the presence of wave forcing	17
2.3.2 Second moment closure	18
2.3.3 Scaling of Langmuir turbulence	20
3 Approaches and methods	21
3.1 Wave effects and numerical modeling	21
3.2 Wave-modified models	24
3.3 Observational methods	25
4 The present study	27
4.1 Objectives and approaches	27
4.2 Numerical tools	27
4.2.1 Data processing and reduction	29
4.3 Instruments and field works	33
4.3.1 MATS	33
4.3.2 Experiments	34
5 Introduction to the papers	37

6 Conclusions and general perspectives **41**
6.1 Main results 41
6.2 Proposed future work 42

References **43**

Chapter 1

Introduction

The Upper Ocean Turbulent Boundary Layer (UOTBL), which is in direct contact with atmosphere above has a great influence on air-sea interaction processes such as the transport of heat, momentum, energy, gas, and other materials, as well as climate change. Approximately 30–40 % of atmospheric carbon dioxide (CO_2) is taken up by the upper ocean, more than 40% of solar radiation is absorbed in the upper roughly 0.5 m below the sea surface. Few meters below the air-sea interface, the heat content of water is nearly the same as that in the atmosphere above (Soloviev et al., 1998). The upper 10–50 m are vertically well mixed with uniform temperature and salinity, and this layer at base is bounded by a sharp change of these quantities which separates the UOTBL from a stable and non-turbulent pycnocline. These highlight the ability of the UOTBL to buffer atmospheric climate changes by the means of thermal and mechanical processes, and to modulate atmospheric fluxes of energy, momentum, and tracers to the deeper water masses, e.g. climate models require sea surface temperature to set the lower boundary condition for the atmosphere (Belcher et al., 2012). Furthermore, the biological and chemical cycles in the ocean are highly connected to the upper ocean mixing. The critical importance of the UOTBL has therefore led to many observational, experimental, and theoretical studies during the last five decades toward better understanding of turbulent mixing and other important processes influencing upper ocean mixing. However, current global climate and UOTBL models, as an integrated system, exhibit substantial systematic errors in the prediction of the underlying physical processes when compared to observations (Fig. 1.1). This may be a result of missing key wave-related processes such as episodic intermittent wave breaking, Langmuir Circulations (LC), and wave-turbulence interactions (Gemmrich and Farmer, 2004; Melville and Matusov, 2002; Sullivan et al., 2004; Thorpe and Humphries, 1980).

The physical structure of the UOTBL covers a wide range of temporal and spatial scales, depending on the magnitude of different forcing conditions which influence the strength of the turbulence such as buoyancy fluxes, bed stress, wind stress, breaking and non-breaking waves, and LC. The buoyancy loss at the surface due to surface cooling, evaporation, and ice freezing at high latitudes results in convection due to unstable surface density stratification. The formation of whitecapping waves as a result of wave breaking leads to a surface layer that is dominated by the generation of Turbulent Kinetic Energy (TKE)(Fig. 1.2) (Terray et al., 1996). Within this layer, dissipation rates of TKE, ε , scale with the rate of energy input from the wind to the waves and a wave-dependent length scale (e.g., wave height or inverse wave number). Then, the

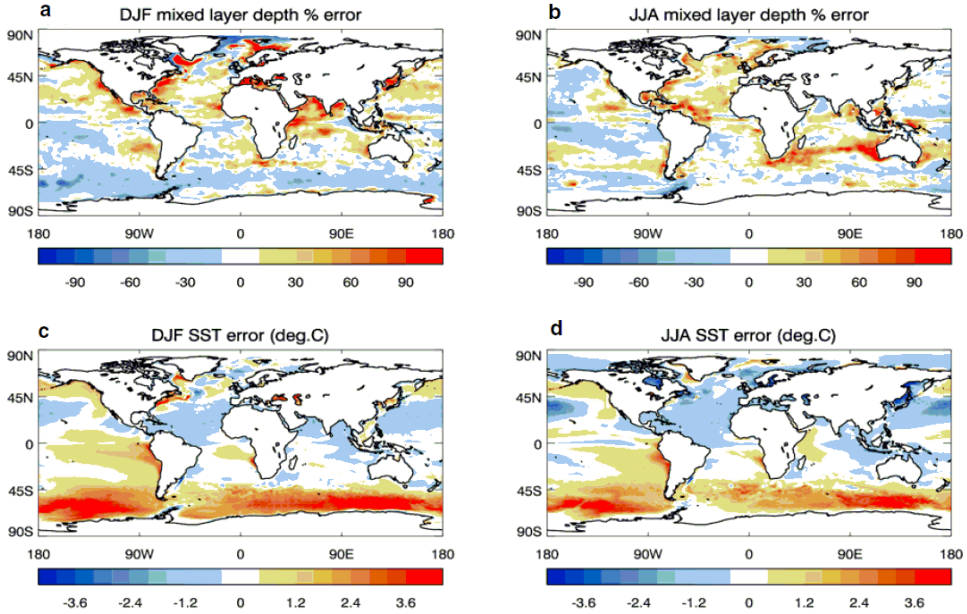


Figure 1.1: Comparison between observed sea surface temperature and mixed-layer depth, and simulation results from the HadGEM3 climate model: a) percentage error in mixed-layer depth in December, January, and February (DJF); b) percentage error in mixed-layer depth in June, July, and August (JJA); c) percentage error in sea surface temperature in DJF; and d) percentage error in sea surface temperature in JJA. Adapted from [Belcher et al. \(2012\)](#).

ocean surface layer in the presence of intermittent wave breaking, and the absence of stratification and rotation can be divided into four sublayers ([Terray et al., 1996](#)):

1. A viscous sublayer (where the normal component of turbulent velocity fluctuations near the density interface is suppressed);
2. A wave breaking sublayer adjacent to the surface (enhanced ε with negligible rates of shear production);
3. A transient sublayer (in which ε decays with depth as z^{-2} , where z denotes the distance below the sea surface);
4. the deepest layer in which the evolution of ε is controlled by local production of energy (law-of-the-wall (LOW)).

Up to 50% of the wave energy lost is used to entrain bubbles into the water column during breaking events, in which momentum and energy are also injected into the water column, down to the depths of the order of a few wave heights ([Lamarre and Melville, 1991](#); [Rapp and Melville, 1990](#)). Furthermore, wave breaking increases the roughness length scale, z_0 , on both sides of the air-sea interface, z_0 being an important scaling parameter for the dynamics of the wave-affected boundary layer. Another

important source of convective wave-related motions in the UOTBL is the large-scale Langmuir circulation which arises as a result of interaction between wind-induced flow and wave-generated Stokes drift. These wave-induced circulations are able to generate high-frequency internal waves in a stratified water column that may significantly enhance turbulent mixing below the surface mixed layer (Polton et al. 2008). Stokes drift can also distort turbulence in the surface layer resulting in an additional wave-induced shear stress under non-breaking wave conditions.

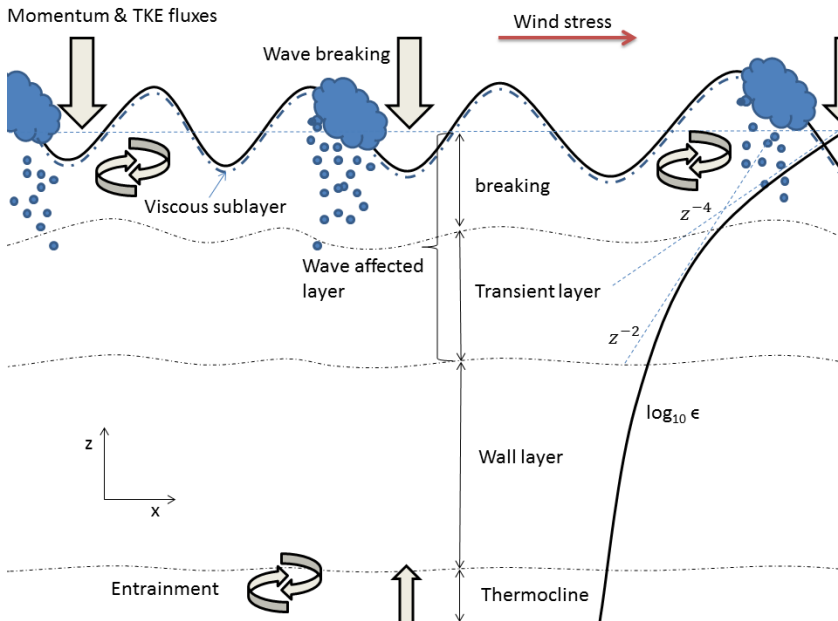


Figure 1.2: Schematic diagram of the vertical structure of the UOTBL resulting from wind forcing and wave breaking. The Stokes drift associated with non-breaking waves also injects energy into the transient layer and deeper into the water column.

Observational evidence of enhanced turbulence and mixing near the wavy surface has motivated several theoretical long-standing investigations toward the coupling between wave, current, and turbulence near the air-sea interface. As mentioned, below the sea surface, surface gravity waves affect turbulence mainly in three ways: 1) second-order wave effects, including the formation of LC by interaction of the wave-induced Stokes drift, \mathbf{u}^s , with the near-surface shear and also a divergence of a stress tensor as a result of wave-averaged effects on the ambient current (radiation-stress); 2) dissipative wave effects (wave breaking and whitecapping); and 3) wave-induced shear stress, $-\overline{u'w'}$, where the overbar denotes a time average, where the waves are not truly irrotational.

Ursell (1950) demonstrated that surface gravity waves cannot induce a steady-state drift current in an inviscid and rotating ocean. This paradox was resolved by Hasselmann (1970) and Pollard (1973) for a non-viscous ocean. For monochromatic waves in a viscous non-rotating fluid, Longuet-Higgins (1953) applied an Eulerian fluid descrip-

tion with curvilinear coordinates to study surface wave effects on the mean momentum transport. Hasselmann (1970) introduced a wave-induced force, $\mathbf{f}_{cor} \times \mathbf{u}^s$, in a rotating fluid due to interaction of the planetary vorticity, \mathbf{f}_{cor} , and wave-induced Stokes drift. Averaging horizontal momentum equations over the wave period results in arising the Coriolis-Stokes forcing (CSF) term in the equations of motions. Huang (1971) demonstrated that the CSF changes the Ekman balance of the upper ocean wind-induced mixing with a combined effect of Coriolis forcing and the divergence of vertical momentum transfer by turbulent stress. Weber (1983b) and Jenkins (1986, 1987) combined both the rotational effects and eddy viscosity to study wave-current interaction. Weber (1983a,b) used a constant eddy viscosity for monochromatic waves, while in the model of Jenkins (1987), the eddy viscosity was treated as vertically varying function of depth for random sea waves. Jenkins (1989) presented a combination between a wave prediction model and a hydrodynamic model by using a second order perturbation expansion in a Lagrangian coordinate system, and vertically varying eddy viscosity for the current field. Teixeira and Belcher (2002) used rapid-distortion turbulence theory to study wave-current interaction. Craik and Leibovich (1976) developed a theory for the large-scale current motion interacting with Stokes drift, resulting in a vortex force (the wave-averaged effect on the vorticity of the current) and Bernoulli head (the effect of the waves on the pressure) (Leibovich, 1983). Wave breaking is a nearly co-existent phenomena with LC that is triggered by non-linear wave-wave, wave-current, and wind-wave interactions. Using a multi-scale technique, Weir (2010) generalized the Craik and Leibovich (1976) theory for the formation of LC based on McWilliams and Restrepo (1999) to include wave breaking. Melsom (1996) proposed a parametrization for the transfer of momentum from breaking waves to the mean flow. Sullivan et al. (2004, 2007) introduced the stochastic breakers forcing terms for the momentum and energy equations, based on field and laboratory observations of breaking waves made by Rapp and Melville (1990) and Melville and Matusov (2002). Theoretical and experimental studies by Arduin and Jenkins (2006), Babanin and Haus (2009), Qiao et al. (2004), and Dai et al. (2010) have shown that non-breaking waves can also transfer energy to the water column.

Development of theory, measurement techniques, and computational facilities have allowed for major advances in the numerical modelling of upper ocean mixing during the past 30 years. A necessary assumption in all these mixed layer models is the existence of a spectral gap between large and small scales. This assumption allows us to introduce averaging operators to separate resolved and unresolved scales. Craig and Banner (1994) and Craig (1996) proposed closure model of a one-dimensional wave-modified model based on the Reynolds-averaged level $2\frac{1}{2}$ Mellor and Yamada (1982) (MY). In their model, they included wave forcing by modifying the TKE flux at the surface. Burchard (2001) treated wave-breaking as a source of TKE using a k - ϵ model. Following the wave-turbulence idea of Kitaigorodskii and Lumley (1983), Benilov and Ly (2002) incorporated wave kinetic energy effects into the TKE budget equation. Mellor (2013) used pressure-slope correlation as the mechanism responsible for transferring momentum and injecting energy into the water column, using MY-type closure model. Sullivan et al. (2004, 2007) followed the idea of direct depth injection of wave energy using stochastic breakers context. They determined the spatial and temporal distributions of breaking waves for momentum and energy exchange. Kudryavtsev et al. (2008) used the same idea of the depth injection of energy and assumed that turbulent

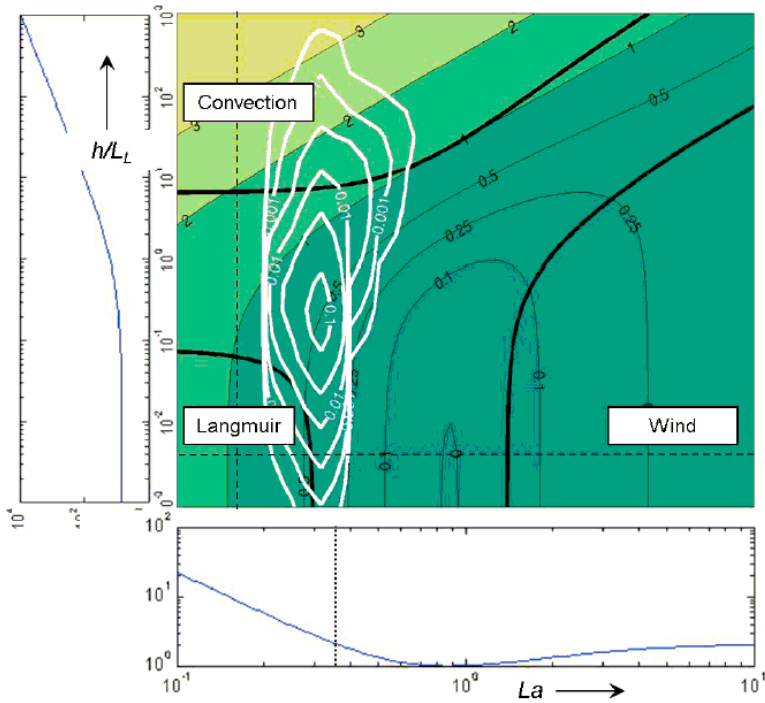


Figure 1.3: Diagram of UOTBL dynamic structures. The coloured contours show the TKE dissipation rate, ϵ , scaled by mixed layer depth and water-side friction velocity which are divided in regions by solid lines to present where single forcing produce greater than 90% of the total ϵ . The white contours show the joint probability density function of Langmuir turbulence number, La , and normalized depth computed for the Southern Ocean winter (JJA). The left and lower panels show the variation of non-dimensional ϵ versus non-dimensional depth, and the variation of non-dimensional ϵ versus La . Here, L_L is the Langmuir stability length scale. Adapted from [Belcher et al. \(2012\)](#).

quantities near the sea surface only depend on the spectral distribution and the size of wave breaking fronts. [Raschle et al. \(2012\)](#) investigated breaking-induced turbulence and its vertical distribution, using the models of [Sullivan et al. \(2007\)](#) and [Kudryavtsev et al. \(2008\)](#). [Belcher et al. \(2012\)](#) investigated gravity wave interactions with turbulent motions and showed that existing turbulent mixing parameterizations lead to substantial errors in the depth of the upper ocean boundary layer in global climate models. They proposed a parametrization for the depth-dependence of ϵ as a function of Langmuir turbulence number, La (Fig. 1.3). [McWilliams et al. \(2012a\)](#) employed a wave-modified K -profile parametrization of eddy viscosity to study Ekman layer variations in the presence of surface gravity waves. Following [Jenkins \(1986, 1987\)](#) and [Tang et al. \(2007\)](#), [Bakhoday-Paskyabi et al. \(2012\)](#) developed an improved k - ϵ model by including CSF and a wave-breaking momentum redistribution term in the equations of motion. [Bakhoday-Paskyabi and Fer \(2014a,b\)](#) conducted a series of model-observation

runs to predict near-surface turbulence variability by including wave effects from different wave-current interaction theories, and introduced a new long-term measuring system for upper ocean turbulence. They used their observed ε to check the skill of the wave-modified model results. Recently, D'Asaro et al. (2014) found consistent agreement between observations (as carried out with a neutrally buoyant Lagrangian profiler) and the predictions of Langmuir turbulence theory both in Lake Washington and at Ocean Station Papa. They concluded that the Craik and Leibovich (1976) mechanism explains nearly the differences between prediction and observation of vertical velocity variance in lake and open ocean.

Objectives

The goal of the investigations described in this thesis is to understand the physics of small-scale processes near the wavy air-sea interface with emphasis on observations of wind-generated waves, wind-induced current and turbulence, and numerical model development for wave-current and wave-turbulence interactions. The principle objectives of this study can be separated into two categories: 1) observations, and data analysis algorithms, and 2) wave-current-turbulence theories and model studies.

The prime observational objectives are to:

1. document and test a new platform to measure turbulence variability in the upper ocean;
2. conduct field experiments covering various atmospheric conditions and wave forcing, to investigate the characteristics of combined wind, wave, and platform interactions. Satisfaction of this objective will provide a reliable assessment of the upper ocean energy components applicable in the environmental monitoring program for development of the offshore wind energy industry;
3. develop data analysis tools for removing wave-induced motion contamination from moving oceanographic and atmospheric sensors, and for estimating the wave energy spectrum from a high-resolution pressure sensor mounted on a moving platform below the sea surface.

The prime modelling objectives are to:

1. investigate theoretically the algebraic turbulence closure equations in the presence of waves, wave-current, and wave-turbulence interactions. This gives us the chance to gain further in-depth understanding of the coupled processes, and improve the scaling of turbulence quantities near the sea surface.
2. apply different parameterizations and scaling of wave interaction with near surface turbulence and conduct a series of model-observation comparisons to confirm the skill of parameterizations.
3. understand and identify the behaviour of current wave-modified turbulence mixing models. To this extent, a wave toolbox has been developed and incorporated

into a turbulent mixing model. This toolbox contains the required options for incorporating the effects of wave-current and wave-turbulence interactions near the wavy air-sea interface.

Chapter 2

Scientific background

In this section, I provide a concise overview of the governing processes in the upper ocean as a framework for the outlined papers in this study.

The basic equations of motion in the Cartesian coordinate (x, y, z) are expressed as

$$\frac{D\mathbf{q}}{Dt} + f_{cor}\hat{z} \times \mathbf{q} = -\frac{1}{\rho_0}\nabla p + \mathcal{B}\hat{z} + \mathbf{F}, \quad (2.1)$$

$$\nabla_h \cdot \mathbf{u} + \frac{\partial w}{\partial z} = 0, \quad (2.2)$$

with tracer equation

$$\frac{\partial \theta}{\partial t} + \mathbf{u} \cdot \nabla_h \theta + w \frac{\partial \theta}{\partial z} = 0, \quad (2.3)$$

and

$$\mathbf{q} = (\mathbf{u}, w); \quad \mathbf{u} = u\mathbf{i} + v\mathbf{j}; \quad \mathcal{B} = g \frac{\rho_0 - \rho}{\rho_0},$$

$$\frac{D}{Dt} = \frac{\partial}{\partial t} + \mathbf{u} \cdot \nabla_h + w \frac{\partial}{\partial z},$$

where $\nabla = (\nabla_h, \partial_z)$ is the *del* function, ∇_h is the horizontal differential operator, $\mathbf{u} = (u, v)$ is the horizontal velocity, u and v are the x and y components of horizontal velocity, respectively, w is the vertical velocity component, f_{cor} is the Coriolis parameter, and D/Dt is the total derivative. \mathbf{i} and \mathbf{j} are the unit vectors in the x and y directions, respectively, \hat{z} is the unit vector in the vertical direction, \mathcal{B} is the buoyancy, ρ is the density, ρ_0 is the reference density, g is the gravitational acceleration, p is the kinematic pressure which includes the hydrostatic contribution, \mathbf{F} denotes the acceleration due to frictional forces, and θ is temperature here. The boundary conditions at the air-sea interface and bottom are expressed as

$$\frac{\partial \zeta}{\partial t} + \mathbf{u} \cdot \nabla_h \zeta - w = 0, \quad \text{at } z = \zeta(\mathbf{x}, t), \quad (2.4)$$

$$w = -\mathbf{u} \cdot \nabla H \quad \text{at } z = -H, \quad (2.5)$$

where $z = H(\mathbf{x})$ describes the bottom topography, $\mathbf{x} = (x, y)$, and ζ denotes the sea surface elevation. The kinematic pressure p in Eq. (2.1) is defined as

$$p = P - \rho_0 g z + P_a, \quad (2.6)$$

where the first term on the right-hand side is the hydrostatic pressure and P_a is the mean atmospheric surface pressure.

One of important assumptions in studying wave-current and wave-turbulence interaction is the existence of spectral gaps between wave, turbulence, and current scales (although finding such gaps empirically is not straightforward) resulting in the partitioning of flow quantities into mean, turbulent, and wave components. This assumption can be meaningful if

$$T' \ll \tilde{T} \ll \bar{T}; \text{ and } X = X' + \tilde{X} + \bar{X}, \quad (2.7)$$

where T' , \tilde{T} , and \bar{T} are the characteristic time scales of turbulent fluctuations, wave motions, and mean motion, respectively; X denotes a generic flow quantity; and X' , \tilde{X} and \bar{X} are the contributions due to turbulent, wave, and mean motions, respectively.

It should be noted that many wave-current-turbulence interaction models use a phase-averaging operator based on the dominant wave period. For a narrow-band wave energy spectrum, it can be assumed that all frequency components beyond the dominant frequency propagate with the dominant wave speed and this averaging works perfectly (Jiang and Street, 1991). Otherwise, the phase-average does not properly separate wave motions from other types of motion.

2.1 Surface gravity waves and wind-wave interaction

The evolution of wave field can be modelled using the energy transport equation:

$$\frac{\partial E(f, \Theta)}{\partial t} + \mathbf{c}_g \cdot \nabla E = S_{in} + S_{ds} + S_{nl}, \quad (2.8)$$

where E is the wave energy spectrum, f is the wave frequency, Θ is the wave direction, \mathbf{c}_g is the wave group velocity, and S_{in} , S_{ds} , S_{nl} are the wind energy input, dissipation, and non-linear wave-wave interaction source terms, respectively. More details can be found in **Paper I**. Over the ocean, as a result of wave-wind interaction, the total overlying wind stress will be composed of wave correlated, mean wind, and turbulent components. If we assume stationary and horizontal homogeneous flow (in a one-dimensional vertical model and for the x -component), we obtain

$$\rho_a \frac{\partial}{\partial z} (\overline{u'w'} + \overline{\tilde{u}\tilde{w}} + \nu \frac{\partial \bar{u}}{\partial z}) = \frac{\partial}{\partial z} [\overbrace{\tau_t + \tau_w + \tau_v}^{\tau_a^x}] = 0, \quad (2.9)$$

where $\boldsymbol{\tau}_a = (\tau_a^x, \tau_a^y)$ is the total stress, ρ_a is the air-side density, and ν is kinematic viscosity. The form drag, τ_w , is determined by the wave-pressure slope covariance as:

$$\tau_w^x = \overline{\tilde{p} \frac{\partial \zeta}{\partial x}}; \quad \tau_w^y = \overline{\tilde{p} \frac{\partial \zeta}{\partial y}}, \quad (2.10)$$

where $\boldsymbol{\tau}_w = (\tau_w^x, \tau_w^y)$ is the wave-induced momentum vector, and \tilde{p} is the surface wave-induced pressure (**Paper V**). Since, the direct measurement of \tilde{p} is difficult near the sea surface, we transform Eq. (2.10) into frequency space to parameterize $\boldsymbol{\tau}_w$. Thus,

using the relation $E = Mc_{ph}$ between energy and momentum, where M denotes the wave-induced momentum, the (infinitesimal) contribution to the form drag for (f, Θ) is calculated from the wind energy input source function as:

$$\boldsymbol{\tau}_w(f, \Theta) = \frac{S_{in}(f, \Theta)}{c_{ph}(f, \Theta)}, \quad (2.11)$$

where c_{ph} is the phase speed, and $\boldsymbol{\tau}_w$ in Eqs. (2.9–2.10) is the integral of all the $\boldsymbol{\tau}_w(f, \Theta)$ in Eq. (2.11). Alternatively, the wave-induced momentum in the presence of breaking crests can be expressed in terms of breaking crest length per unit area. Assuming that the surface gravity waves can be described by Fourier components and that waves of amplitude greater than a critical amplitude will break, Kudryavtsev and Makin (2001, 2002) used the pressure drop at the forward face of breaking fronts to modify the form drag by including the effects of breaking crests.

2.2 Wave-current interaction

In the upper ocean boundary layer, wind-generated surface gravity waves, and currents coexist and interact prominently resulting in ultimately turbulent mixing in the UOTBL. There is a growing interest in the role of (phase-averaged) wave-current interaction in the dynamics of the upper ocean boundary layer. Basically, I can classify the mathematical representations of wave-current interaction into three categories:

1. the "vortex force" that was initially derived by Garrett (1976) to study the formation of coherent Langmuir cells through the Stokes drift shear interaction with the wind-driven near-surface current. The vortex force effect includes a Bernoulli head (adjustment to the pressure), and a vortex force (interaction between vorticity and Stokes drift);
2. the "radiation stress" concept presented by Longuet-Higgins and Stewart (1962, 1964) and many other investigators, in the depth-integrated paradigm. This wave-induced effect appears in the governing equations as the divergence of a stress tensor;
3. the wave-current interaction concept in the Lagrangian or hybrid Eulerian-Lagrangian reference frames (Aiki and Greatbatch (2012), Ardhuin et al. (2008), Mellor (2003), Jenkins (1989), Jenkins (1987), Jenkins (1986), Weber (1983b), Weber (1983a)).

The theoretical formulations of the first two categories depend on the representation of the advection term in Eq. (2.1). In the vortex force representation, it is formulated as

$$(\mathbf{q} \cdot \nabla) \mathbf{q} = \frac{1}{2} \nabla (\mathbf{q} \cdot \mathbf{q}) - \mathbf{q} \times \boldsymbol{\omega},$$

where $\boldsymbol{\omega} = \nabla \times \mathbf{q}$ is the vorticity and $\mathbf{q} = (\mathbf{u}, w)$ is the Eulerian three-dimensional velocity. In the radiation stress representation, the advection term is expressed by

$$(\mathbf{q} \cdot \nabla) \mathbf{q} = \nabla \cdot (\mathbf{q}\mathbf{q}) + \mathbf{q}(\nabla \cdot \mathbf{q}).$$

Although these two types of theoretical representations for wave-current interaction are highly consistent, their applications and numerical model results may perform differently. The radiation stress representation is usually used for generation of alongshore currents and wave set-up, whereas the vortex force representation is used to explain LC generation and evolution. In this section, I re-formulate the governing equations of motions using these three types of wave forcing, addressing appropriate references wherever required.

2.2.1 Vortex force (vertically resolved approach)

McWilliams and Restrepo (1999) and McWilliams and Lane (2004) studied the large-scale dynamics of the wave-driven ocean circulation at shelf to basin scales. Lane et al. (2007) conducted a comparison between the "vortex force" model (VF) and the "radiation stress" formulation (RS) for wave-current interaction. In addition to the conservative effects of VF and Bernoulli head, there are important non-conservative effects due to depth-induced breaking (and whitecapping as the short-lived, and random episodes) near the surface and frictional wave dissipation near the bottom. In their derivations, McWilliams and Lane (2004) developed representations for the conservative dynamics of currents and gravity waves. Restrepo (2007) addressed the non-conservative whitecapping effects on wave-current interactions using a parametric representation of breaking as a diffusion term (Langevin-like stochastic differential equations).

Here, for brevity I will not show the interactions between dissipative effects on both wave scales and the general wave-current interaction evolution equations. The main goal of the current section is to provide a robust derivational methodology for wave-current interaction, based on the Craik and Leibovich (1976) approach. It is emphasized that resolving both wave, mean, and turbulent scales is computationally very expensive, and it is thus conventional to study the resultant large-scale wave-current interaction dynamics in terms of some filtered wave quantities appearing in the resultant governing equations, with the provision that they retain as many dynamical properties as possible, for example conservation. In this regard, I introduce two independent types of averaging: $(\overline{\cdot})$ which is used for filtering out the fast time scales, and $(\langle \cdot \rangle)$ which is applied over the slow time scales. For instance, these two scales separate the velocity field into rapidly and slowly varying components in time, t_f and t_s , respectively. If \mathbf{X} is a generic flow quantity, we have $\mathbf{X} = \langle \mathbf{X} \rangle + \widehat{\mathbf{X}}$.

While much of the work in this section is a re-formulation of previous works, some minor modifications are carried out to incorporate the Coriolis effect on the multiple-scale method used by Weir (2010). The tracer equations are omitted from this section for the sake of brevity. Eqs. (2.1-2.2) are non-dimensionalized according to

$$\begin{aligned} (\mathbf{x}, z) &\longrightarrow L_0^{-1}(\mathbf{x}, z), \\ t &\longrightarrow \left(\frac{U_0}{L_0}\right)t, \\ \mathbf{q} &\longrightarrow U_0^{-1}\mathbf{q}, \\ P &\longrightarrow (\rho_0 U_0^2)^{-1}P, \end{aligned}$$

where the quantities on the right-hand sides are non-dimensional. $L_0 = k_0^{-1}$ is the characteristic depth, $U_0 = \sigma_0 k_0^{-1}$ is the characteristic velocity, $\varepsilon = a_0 k_0$ is the typical wave

steepness, where a_0 and k_0 are the characteristic wave amplitude and wavenumber, respectively. σ_0 is the characteristic angular frequency satisfying the deep water dispersion relation $\sigma_0^2 = gk_0^2$. Furthermore, the Coriolis term is scaled by the characteristic planetary vorticity Ω_0 . Assuming $U_0k_0^{-1} \ll 1$, the rapid and slow time scales are defined as a linear function of wave time scale, t_w , as:

$$t_s = \varepsilon_c t_w \quad \text{and} \quad t_f = \varepsilon_t^{-1} t_w, \quad (2.12)$$

where $\varepsilon_c = \tilde{T}/\bar{T}$ and $\varepsilon_t = T'/\bar{T}$. The three-dimensional, non-dimensional velocity field, \mathbf{q} , is expressed as an expansion with $\mathcal{O}(\varepsilon)$ wave velocity and $\mathcal{O}(\varepsilon^2)$ current ($\mathbf{q} = \varepsilon \tilde{\mathbf{q}} + \varepsilon^2 \mathbf{v}$). Taking the curl of Eq. (2.1), considering the irrotationality of wave field ($\nabla \times \mathbf{q} = \varepsilon^2 \nabla \times \mathbf{v} = \varepsilon^2 \boldsymbol{\omega}$), and averaging over the fast scales, we find an expression for the non-dimensional vorticity $\boldsymbol{\omega}$. Substituting the perturbation expansion $\hat{\mathbf{v}} = \mathbf{v}_0 + \varepsilon \mathbf{v}_1 + \dots$ and $\hat{\boldsymbol{\omega}} = \boldsymbol{\omega}_0 + \varepsilon \boldsymbol{\omega}_1 + \dots$ for velocity and vorticity, we obtain a set of equations. For instance, the zero-order balance for vorticity is (McWilliams and Restrepo, 1999):

$$\frac{\partial \boldsymbol{\omega}_0}{\partial t_s} = \nabla \times (\mathbf{u}^s \times \boldsymbol{\omega}_0) + \nabla \times (\mathbf{v}_0 \times \boldsymbol{\omega}_0) + \nabla \times (\mathbf{v}_0 \times 2\boldsymbol{\Omega}) + La \nabla^2 \boldsymbol{\omega}_0 + \dots, \quad (2.13)$$

where La is the Langmuir turbulence number (**Paper IV**), $\boldsymbol{\Omega} = (0, 0, f_{cor}/2)$ is the angular velocity vector of Earth's rotation, and $\mathbf{u}^s = (u^s, v^s, 0)$ is the Stokes drift:

$$\mathbf{u}^s = \left\langle \int^{t_w} \tilde{\mathbf{q}}(\cdot, s) ds \cdot \nabla \tilde{\mathbf{q}} \right\rangle, \quad (2.14)$$

with a dimension scale of $\varepsilon^2 \sigma_0/k_0$. The current velocity equations are then given by setting $\mathbf{q} = \mathbf{v}_0$ and $t_s = t$ as

$$\frac{\partial \mathbf{q}}{\partial t} + \mathbf{q} \cdot \nabla \mathbf{q} = \mathbf{u}^s \times (\nabla \times \mathbf{q} + 2\boldsymbol{\Omega}) - \nabla \Pi + La \nabla^2 \mathbf{q} + \dots, \quad (2.15)$$

where wave-modified pressure (Bernoulli head) is given by

$$\Pi = p + \frac{1}{2} (\mathbf{q} + \mathbf{u}^s)^2.$$

The term $\mathbf{u}^s \times (\nabla \times \mathbf{q})$, the Craik and Leibovich (1976) vortex force, is a result of the interaction between the wave-induced Stokes drift and the wind-driven shear current, generating Langmuir turbulence.

2.2.2 Radiation stress (vertically integrated approach)

In this section, all quantities are presented in their dimensional forms, and I will clarify changes whenever it is required. I examine the vertically-integrated momentum budget by accounting for both mean current and wave motions. For simplicity, the turbulence contribution is ignored. The mean flow is then divided into Eulerian mean and wave motions.

The radiation stress as the net flux of momentum due to the surface wave field was first introduced by Longuet-Higgins and Stewart (1962, 1964) as a vertically integrated tensor without any vertical distribution. Haas et al. (2003) introduced a new

splitting algorithm to study vertical variations of horizontal velocities. Their formulations were derived from depth-integrated and wave-averaged momentum equations. Xia et al. (2004) extended the vertically integrated RS to the vertically varying by utilizing linear wave theory. Mellor (2003) derived a formulation for the depth-dependent RS, again using linear wave theory for the vertically Lagrangian three-dimensional equations of motion. Ardhuin and Elfouhaily (2004) discovered a phenomenon for producing deep mean current when Mellor (2003) RS was employed (in the presence of a bottom slope or wave field gradients). Mellor et al. (2008) improved the representation of RS and proposed a new representation for the depth-dependent RS. In this section, I reformulate the vertically-integrated wave-current interaction problem using approaches proposed by Smith (2006), Lane et al. (2007), and Broström et al. (2008).

Upon vertically integrating Eq. (2.1) from the bottom ($z = -H$) to the surface ζ , using boundary conditions (Eqs. 2.4 and 2.5), and splitting the flow into mean and wave components ($u_i = \bar{u}_i + \tilde{u}_i$, $p = \bar{p} + \tilde{p}$, and $\zeta = \bar{\zeta} + \tilde{\zeta}$), the time-averaged equations are obtained as:

$$\begin{aligned} \frac{\partial \bar{T}_i}{\partial t} + \frac{\partial \tilde{T}_i}{\partial t} &= -\frac{\partial}{\partial x_j} \left(\int_{-H}^{\bar{\zeta}} \bar{u}_i \bar{u}_j dz + \int_{-H}^{\bar{\zeta}} \bar{p} \delta_{ij} dz \right) - \frac{\partial S_{ij}}{\partial x_j} \\ &\quad - f_{cor}(\hat{z} \times \bar{T})_i - f_{cor}(\hat{z} \times \tilde{T})_i + \tilde{p}(z = -H) \frac{\partial H}{\partial x_i} \\ &\quad + [\bar{p}(z = \bar{\zeta}) - \tilde{p}(z = \bar{\zeta})] \frac{\partial \bar{\zeta}}{\partial x_i} + \dots, \end{aligned} \quad (2.16)$$

where

$$\begin{aligned} \bar{T}_i &= \int_{-H}^{\bar{\zeta}} u_i dz; \quad \text{and} \quad \tilde{T}_i = \int_{\bar{\zeta}}^{\zeta} u_i dz, \\ S_{ij} &= \frac{\int_{-H}^{\zeta} (\tilde{u}_i \tilde{u}_j + \tilde{p} \delta_{ij}) dz}{\int_{\bar{\zeta}}^{\zeta}} - \frac{\int_{\bar{\zeta}}^{\zeta} (u_i u_j + P \delta_{ij}) dz}{\int_{\bar{\zeta}}^{\zeta}}. \end{aligned} \quad (2.17)$$

The first term on the right-hand side (RHS) of Eq. (2.17) is the radiation stress as defined by Longuet-Higgins and Stewart (1962, 1964). From the left-hand side (LHS) of Eq. (2.16), the wave-current interaction equation can be connected to the wave evolution (Eq. 2.8). Here, I briefly list the required steps and refer to Smith (2006) for further details. The radiation stress may be expressed using an estimate given by Longuet-Higgins and Stewart (1962) and Longuet-Higgins and Stewart (1964). Then, the conservation of wave action together with conservation of wavenumber result in a wave-momentum evolution equation that is then substituted to the LHS of Eq. (2.16). The resulting mean current equation includes a new form of wave-induced force (a vortex term) obtained by accounting for wave refraction by current shear (Smith, 2006).

2.2.3 Hybrid approaches

Traditionally, a single coordinate system is employed for both vertical and horizontal coordinates in ocean circulation models. In the presence of a moving wavy surface

boundary, however, a number of alternative coordinate systems have been proposed. In particular, differing vertical coordinates are chosen, in order to improve the representation of the surface elevation, which is poorly resolved by conventional model grids. Mellor (2003) proposed a σ -coordinate in the vertical domain to study wave-current interaction (Mellor et al., 2008). Aiki and Greatbatch (2012) used a vertical Lagrangian coordinate system to investigate the same problem. However, two important questions arise when using such hybrid coordinate systems: how do the wave-induced terms in the hybrid systems compare with those in the single coordinate models?, and how meaningful and relevant are the additional wave-induced terms obtained in the hybrid approaches? Here, I briefly discuss these concerns by re-formulating the vertically Lagrangian coordinate system proposed by Aiki and Greatbatch (2012) as a double averaging hybrid approach.

Let us call the single coordinate frame with independent variables x , y , z , and t , a z -system. The generalized vertical coordinate system, g -system, is defined using x , y , and t similar to those of the z -system, but vertical coordinate is defined as a function of s rather than z :

$$z = z(x, y, s, t). \quad (2.18)$$

Now, any quantity can be expressed in the g -system using Eq. (2.18) and the chain rule. For example, the horizontal equation of motion (Eq. 2.1) can be transferred to the g -system as

$$\frac{D\mathbf{u}}{Dt} + f_{cor} \hat{z} \times \mathbf{u} = -\frac{1}{\rho} \nabla^g P + \frac{1}{\rho} \left(\frac{\partial s}{\partial z} \right) (\nabla^g z) \frac{\partial P}{\partial s} + \mathbf{F}, \quad (2.19)$$

where ∇^g is the horizontal *del* function in the g -system. Using the following relations

$$w = \left(\frac{\partial z}{\partial t} \right)_g + \mathbf{u} \cdot \nabla^g z + s \frac{\partial z}{\partial s}, \quad (2.20)$$

$$\nabla_z \cdot \mathbf{u} = \nabla^g \cdot \mathbf{u} - \left(\frac{\partial s}{\partial z} \right) (\nabla^g z) \cdot \frac{\partial \mathbf{u}}{\partial s}, \quad (2.21)$$

the continuity equation can be obtained in the g -system:

$$\nabla^g \cdot \mathbf{u} + \frac{\partial s}{\partial s} = \left[\frac{\partial}{\partial t} \left(\rho \frac{\partial z}{\partial s} \right) \right]^g + \frac{\partial}{\partial s} \left(\rho s \frac{\partial z}{\partial s} \right) = 0. \quad (2.22)$$

Aiki and Greatbatch (2012) used Favre averaging (conventional for compressible flows) to perform separation of scales by multiplying the incompressible version of Eq. (2.19) by the layer thickness in the g -system and decomposing the velocity and pressure fields into Favre-averaged and fluctuation components. Their hybrid system leads to two wave-induced terms: the Favre-averaged Reynolds stress, and a form stress, respectively. Their technique results further in a wave-induced quasi-Stokes drift, closely related to the Stokes drift (2.14).

Another method which provides a hybrid Eulerian-Lagrangian formulation is the Generalized Lagrangian Mean (GLM) formulation of Andrews and McIntyre (1978) with a (on average) stationary coordinate system. In this approach, the mean fluid velocity at a particular position is expressed by the mean velocity drift of fluid particles. Arduin et al. (2008) used an exact GLM wave-averaged momentum equations of

Andrews and McIntyre (1978), and under the hypothesis of small surface slope, they provided analytical expressions for the wave-induced terms to second order. Through the change of vertical coordinate, they obtained *glm2z*-RANS equations in cartesian coordinates.

2.3 Wave-turbulence interaction

Wave-turbulence interactions in the presence of surface currents have been the subject of many theoretical (Babanin and Haus, 2009; Jiang and Street, 1991; Kitaigorodskii et al., 1983), experimental (Fer and Bakhoday-Paskyabi, 2014; Gemmrich and Farmer, 2004; Rapp and Melville, 1990), and numerical studies (Burchard, 2001; Craig, 1996; Craig and Banner, 1994). The present understanding of this complex coupled dynamical system is, however, rudimentary due mainly to the scarcity of accurate measurements and the lack of appropriate stable platforms (to carry oceanographic sensors in the UOTBL), and appropriate data analysis techniques which allow for separation of wave motions from turbulent components of current. Different aspects of the coupled wave and turbulence in the surface zone can be summarized as follows:

1. near the sea surface, most of turbulent energy is concentrated in frequencies lower than the wave-affected frequency band;
2. there exists an inertial subrange with a slope of $-5/3$ for the turbulent spectra similar to those observed in the vicinity of a solid boundary;
3. wave orbital velocities, together with the mean current, advect turbulent eddies past a fixed point;
4. surface gravity waves dissipate energy locally via wave breaking into the water column (with depths proportional to the wave height), resulting in a substantial enhancement of TKE and its dissipation near the sea surface;
5. surface waves are not perfectly irrotational, i.e., the horizontal and vertical velocities are not in quadrature and there exist wave-induced downward Reynolds stresses;
6. wave energy can be transferred to the turbulent field associated with the attenuation of surface waves and non-breaking wave effects;
7. wave-induced transport of TKE can be another mechanism associated with wave-turbulence interaction.

Based on field measurements in Lake Ontario, Kitaigorodskii and Lumley (1983) found dramatically increased levels of both the TKE and its dissipation, ϵ , near the sea surface below wind-generated waves. ϵ was nearly 2 orders of magnitude larger than the value predicted by LOW. They suggested that "wave-turbulence interaction" can be responsible for such enhancement. They also argued that there is a wave-induced bump in the turbulent spectra with a peak at the dominant wave frequency. Lumley and Terray (1983) analysed the measurements of Kitaigorodskii and Lumley (1983) by

filtering the wave-induced motions from the total velocity. They found that there exists an inertial subrange with a $-5/3$ slope away from the dominant wave frequency with an apparent enhancement of energy at high frequencies (Terray and Bliven, 1985). Magnaudet and Thais (1995) and Thais and Magnaudet (1996) separated the rotational and irrotational components of the wave orbital velocities from the turbulent fluctuations. They showed that the rotational component of the wave orbital velocity plays a substantial role in the exchange of energy between the mean shear flow and wave motions. Cheung and Street (1988) and Thais and Magnaudet (1996) suggested that an important part of wave-turbulence interaction results from wave-induced stress linked to the rotational characteristics of the wave motions. In addition to the wave stress, departure from potential flow, and vertical transport of Wave Kinetic Energy (WKE) by turbulent motions, Anis and Moum (1995) proposed that wave-turbulence interaction can also occur as a result of low-frequency wave motions (swell). Teixeira and Belcher (2002) studied the interaction between a monochromatic irrotational wave field and weak near-surface turbulence. They attributed the generation of LC and wave-induced shear stresses as a result of the distortion of turbulence by the Stokes drift. They also suggested that these stresses perform work against the straining of the wave motions, resulting in conversion of WKE into TKE over many wave periods.

2.3.1 TKE budgets in the presence of wave forcing

Before dealing with the TKE budget equations, I briefly explain how momentum transfer can occur through wave-turbulence interaction. The wave motions are separated from mean and turbulent flows using a phase-averaging operator. The time-averaged momentum equations contain the following wave-induced, turbulent, and mixed Reynolds stresses:

$$\bar{u}_i \bar{u}_j + \overline{\tilde{u}_i \tilde{u}_j} + \overline{u'_i u'_j} + \overline{\tilde{u}_i \tilde{u}'_j}. \quad (2.23)$$

Assuming horizontal homogeneity and ignoring the horizontal gradient contributions, the wave-induced terms such as $\overline{\tilde{u}u'}$, $\overline{\tilde{w}w'}$, $\overline{\tilde{u}w'}$, and $\overline{\tilde{w}u'}$ cannot play an important role in momentum exchange (Jiang and Street, 1991). However, the terms $\overline{\tilde{u}\tilde{w}}$ and $\overline{\tilde{v}\tilde{w}}$ may make a significant contribution to extracting momentum from the wave field (Section 2.1).

I assume that the mean flow is in the x -direction and $\bar{u} = (u, 0, 0)$. The kinetic energy of the mean flow (MKE), of the wave orbital flow (WKE), and of turbulence (TKE) are then defined by $\bar{k} = \frac{1}{2}(\bar{u}\bar{u})$, $\tilde{k} = \frac{1}{2}(\tilde{u}_i \tilde{u}_j)$, and $k' = \frac{1}{2}(u'_i u'_j)$, respectively. Following Anis and Moum (1995), and using Eq (2.1), the time average of the triple decomposed flow field is

MKE:

$$\frac{D\bar{k}}{Dt} = \overline{u'w'} \frac{\partial \bar{u}}{\partial z} + \overline{\tilde{u}\tilde{w}} \frac{\partial \bar{u}}{\partial z} - \frac{\partial}{\partial z}(\overline{u'w'u}) - \bar{u} \frac{\partial}{\partial x} \left(\frac{\bar{p}}{\rho} \right), \quad (2.24)$$

WKE:

$$\frac{D\tilde{k}}{Dt} = \overline{u'_i u'_j} \frac{\partial \tilde{u}_i}{\partial x_j} - \overline{\tilde{u}\tilde{w}} \frac{\partial \bar{u}}{\partial z} - \frac{\partial}{\partial z}(\overline{u'_i u'_j \tilde{u}_i}) - \frac{\partial}{\partial z} \left(\frac{\overline{\tilde{p}\tilde{w}}}{\rho} \right) - \frac{\partial}{\partial z}(\overline{\tilde{k}\tilde{w}}), \quad (2.25)$$

TKE:

$$\frac{Dk'}{Dt} = \underbrace{-\widetilde{u'_i u'_j} \frac{\partial \bar{u}_i}{\partial x_j}}_1 - \underbrace{\bar{u}' w' \frac{\partial \bar{u}}{\partial z}}_2 - \frac{\partial}{\partial z} \left[(\bar{k}' w' + \bar{k}' \bar{w}) + \left(\frac{p'}{\rho} w' \right) \right] - \varepsilon, \quad (2.26)$$

where ε is the dissipation rate of TKE, term 1 indicates the direct production of TKE as a result of periodic wave shear interaction with wave-modulated Reynolds stress (according to the analysis of Kitaigorodskii et al. (1983) and Kitaigorodskii and Lumley (1983) the contribution of term 1 is negligible in the case of irrotational waves), term 2 is the production of TKE by mean shear, and $\partial(\bar{k}' w')/\partial z$ is the turbulence diffusion (vertical flux of energy). Generally this term plays an important role in the budget equation when the rotational wave velocity component is significant or when there exists a strong vertical gradient of wave orbital velocities (in large-scale plunging waves, the potential component, irrotational waves, may contribute in diffusion of energy) (Thais and Magnaudet, 1996). $\widetilde{u'_i u'_j}$ is the wave-modulated turbulent momentum flux, i.e. the part of the Reynolds stress tensor which has phase correlation with waves. The pressure-diffusion contribution is $\partial(\bar{p}' w'/\rho)/\partial z$, and term $\partial(\bar{k}' \bar{w})/\partial z$ is the vertical transport of wave-modulated TKE by the wave vertical velocity (this approach is explained in **Paper V**).

In the absence of breaking wave crests, the enhanced ε as a result of wave-turbulence interaction may be explained in two ways: 1) Non-zero wave-induced stress, $-\bar{u}' \bar{w}'$, results in the wave-induced production term in Eq. (2.24) which converts the wave energy to the mean current. Gradually, this energy is transferred to the TKE through the mean shear production term; 2) The wave-modulated Reynolds stresses do work against the shear of the (rotational) wave component as represented in Eq. (2.26).

2.3.2 Second moment closure

The turbulent fluxes in Eqs (2.24)–(2.26) are obtained using turbulence closure schemes. In this section, I present briefly how to calculate these fluxes diagnostically for a wave-modified model with the vortex force effect.

To characterize the turbulent flow, the phase-averaged quantities in Eq. (2.15) are decomposed into ensemble-averaged (\bar{u}_i) and turbulent components (u'_i). Then the prognostic equations for turbulent Reynolds stress, $\overline{u'_i u'_j}$ is assigned by assuming horizontal homogeneity. As an example, the final form for the momentum flux budget is given by (Harcourt, 2013):

$$\begin{aligned} \frac{\partial \overline{u'_i u'_j}}{\partial t} &= P_{ij} + P_{ij}^s - \underbrace{\alpha(g \delta_{3j} \overline{u'_i \theta'} + g \delta_{3i} \overline{u'_j \theta'})}_1 - \underbrace{2\nu \frac{\partial u'_i}{\partial x_k} \frac{\partial u'_j}{\partial x_k}}_2 \\ &- \underbrace{\frac{\partial}{\partial x_k} \left[\overline{u'_i u'_j u'_k} - \nu \frac{\partial \overline{u'_i u'_j}}{\partial x_k} + \overline{p' (\delta_{jk} u_i + \delta_{jk} u_j)} \right]}_3 \\ &- \underbrace{2\Omega_k (\varepsilon_{jkl} \overline{u'_i u'_l} + \varepsilon_{ikl} \overline{u'_j u'_l})}_4 + \Pi_{ij}, \end{aligned} \quad (2.27)$$

where f_j is the j th component of the Coriolis vector, ν is the molecular viscosity, and

$$P_{ij} = - \left[\overline{u'_j u'_k} \frac{\partial U_i}{\partial x_k} + \overline{u'_i u'_k} \frac{\partial U_j}{\partial x_k} \right], \quad (2.28)$$

$$P_{ij}^s = - \left[\overline{u'_j u'_k} \frac{\partial u_k^s}{\partial x_i} + \overline{u'_i u'_k} \frac{\partial u_k^s}{\partial x_j} \right], \text{ and} \quad (2.29)$$

$$\Pi_{ij} = \overline{p' \left(\frac{\partial u'_i}{\partial x_k} + \frac{\partial u'_j}{\partial x_k} \right)}, \quad (2.30)$$

are the production rates by mean velocity shear, by wave-induced Stokes shear, and by pressure-strain redistribution processes, respectively. Equation (2.27) includes various mechanisms for controlling the Reynolds stress balance. In this equation, term 1 denotes buoyancy production or consumption, term 2 is the viscous dissipation, term 3 is redistribution by the return to isotropy, and term 4 represents Coriolis effects. It can be seen that Eq. (2.27) contains both second-order and third-order moments including the viscous dissipation, the turbulence transport, and the pressure-strain terms. These should be prescribed to close the equations. Following Mellor and Yamada (1982), Kantha and Clayson (1994), and Harcourt (2013), and using an algebraic approach, we can obtain representations of Reynolds stresses without solving the full second-moment closure equations, while retaining the effects of anisotropic forcing. For instance, the $u'w'$ component of momentum flux is thus:

$$\overline{u'w'} = -3A_1 l q^{-1} \left\{ \begin{array}{l} [q^2 \gamma^* + 6A_1 l q^{-1} (\alpha g \overline{w'\theta'} - \overline{u'w'} \partial_z u^s - \overline{v'w'} \partial_z v^s)] \partial_z \bar{u} \\ + [q^2 \gamma^* - 6A_1 l q^{-1} \overline{u'w'} \partial_z \bar{u}] \partial_z u^s \\ - 3A_1 l q^{-1} [\overline{u'w'} \partial_z \bar{v} + \overline{v'w'} \partial_z \bar{u}] \partial_z v^s \\ + 3\alpha g A_2 l q^{-1} [\overline{u'w'} \partial_z \bar{\theta} + (1 - C_2) \overline{w'\theta'} \partial_z \bar{u} - C_2^s \overline{w'\theta'} \partial_z u^s] \end{array} \right. \quad (2.31)$$

where $\gamma^* = (1 - 6A_1/B_1 - 3C_1)/3$, C_2 and C_2^s are model constants, and ∂_z denotes the derivative with respect to z . In general, the momentum and heat flux equations can be closed by the means of closures in the presence of wave effects, for example:

$$\overline{\mathbf{u}'w'} = -K_m \frac{\partial \bar{\mathbf{u}}}{\partial z} - K_m^s \frac{\partial \mathbf{u}^s}{\partial z}; \quad \overline{\theta'w'} = -K_h \frac{\partial \bar{\theta}}{\partial z}, \quad (2.32)$$

and

$$K_m = lqS_m; \quad K_m^s = lqS_m^s; \quad K_h = lqS_h,$$

where l is the mixing length, q is the turbulent velocity, and S_m , S_m^s and S_h are the stability functions (Harcourt, 2013). Alternatively, McWilliams et al. (2012b) proposed the following closure for the momentum flux:

$$\overline{\mathbf{u}'w'} = -K'_m \left(\frac{\partial \bar{\mathbf{u}}}{\partial z} + \frac{\partial \mathbf{u}^s}{\partial z} \right), \quad (2.33)$$

where the wave-modified eddy viscosity is defined as

$$K'_m = lqS_m + lqS_m^s. \quad (2.34)$$

For more information, I refer readers to Harcourt (2013).

2.3.3 Scaling of Langmuir turbulence

Using results from a large eddy simulation model and Eq. (2.27), Belcher et al. (2012) conducted a diagnostic study to resolve the observed underestimation of mixing in the UOTBL as a result of the neglect of important contributions from physical, wave-induced (Langmuir turbulence), processes from current parameterizations of the UOTBL. As shown in Fig. 1.2, the turbulence structure is influenced substantially by wave breaking in the regions close to the sea surface. However, Belcher et al. (2012) suggested that in the middle of mixed layer, the dissipation rate of TKE can be parameterized as a linear combination of the dissipation from wind, waves, and buoyancy forcing:

$$\varepsilon = \frac{u_{*w}^3}{h} \Upsilon \left(\frac{z}{h}, La, \frac{h}{L_L} \right), \quad (2.35)$$

where u_{*w} is the water-side friction velocity, Υ is a universal function, L_L is the Langmuir stability length, and h is the mixed layer depth. They parameterized ε at $z = h/2$ as

$$\frac{\varepsilon_B(z = h/2)}{u_{*w}^3/h} = A_s + A_L La^{-2} + A_c La^{-2} \frac{h}{L_L}, \quad (2.36)$$

where ε_B denotes the parametrization of the dissipation rate at $z = h/2$, as suggested by Belcher et al. (2012), $A_s = 2(1 - \exp(-La/2))$, $A_L = 0.22$, and $A_c = 0.3$. Figure 1.3 shows contours of $\log_{10}(\varepsilon/\varepsilon_B)$ in the diagram of regions in the $(La)-(h/L_L)$ plane.

Chapter 3

Approaches and methods

The existing gaps in our understanding of upper ocean mixing may reflect the inaccuracy of large-scale ocean circulation models to model small-scale processes such as dissipation rates of TKE, ε , in the presence of surface wave effects. The lack of accurate microstructure measurement systems in the vicinity of the wavy air-sea interface is one of the obstacles to improving our understanding. However, a number of emerging elegant theoretical, numerical, and experimental studies are closing this gap. The following sections will briefly review the relevant progress, focusing mainly on the small-scale parameterizations, modelling, and measurements.

3.1 Wave effects and numerical modeling

Rapp and Melville (1990) conducted laboratory measurements of wave breaking, in which it was determined that for spilling breakers, breaking accounted for approximately 10% of the wave energy loss, whereas the corresponding proportion for plunging breakers was 25%. In Melville and Matusov (2002) experiments, it was found that approximately 90% of the wave breaking energy is dissipated by turbulence within four wave periods, and the remaining energy contributes to the generation process of a coherent "roller" structure scaled with the significant wave height. Terray et al. (1996) proposed a parametrization of enhanced turbulence below breaking waves using energy input from wind to waves, significant wave height, H_s , and depth. The dissipation rate ε in the wave-affected surface layer can be written as (Gerbi et al., 2009):

$$\varepsilon = 0.3G_t \frac{u_{*w}^3 H_s}{z^2},$$

where G_t is a dimensionless parameter defined as the ratio between the water-side friction velocity, u_{*w} , and the energy flux from wind to wave ($90 < G_t < 250$). We have used this parametrization in **Papers I, II, IV, and V**.

From measurements of ocean temperature made at 0.67 m below the sea surface, Gemmrich and Farmer (1999) observed that cooling events, accompanied by increased mixing, occurred between breaking events. Gemmrich and Farmer (2004) reported the correlation between enhanced dissipation rate of TKE and breaking events and their corresponding wave breaking energy lost in the surface layer. However, as much as 50% of the breaking wave energy is also spent on work done in the submersion of

bubbles (Loewen and Melville, 1991). Gemmrich (2010) measured ε in the field using an acoustic profiling system looking upward to the wave crest located above the mean sea level, and found that turbulence was enhanced substantially in the crest regions, and was more energetic than those observed previously.

Let us assume $S_{ds} = S_{brk} + S_{vis} + S_{wti}$, where S_{brk} denotes the energy loss associated with breaking waves, S_{vis} is the energy loss due to viscous force, and $S_{wti} \sim \int_{-z}^0 \bar{u}\bar{w}\partial\bar{u}/\partial z$ is the energy loss due to wave-turbulence interaction, where \bar{u} and \bar{w} are the horizontal and vertical components of the wave orbital velocity. Following Duncan (1981) and Phillips (1985), the breaking energy dissipation rate per length of breaking front, ε_l , can be scaled, especially when wave breaking is the principle source of TKE, according to:

$$\varepsilon_l = \frac{b\rho_w c^5}{g} = \frac{S_{brk}}{\Lambda(c)}, \quad (3.1)$$

where c is the speed of the breaking crest front, $\Lambda(c)$ is the length of breaking crest per unit area, and b is an empirical breaking parameter which depends on wave age, wave slope, and other wave parameters. Sullivan et al. (2004) and Sullivan et al. (2007) developed a model of breaker impulses for the injection of momentum, M_b , and energy, ε_b (the transport terms in Eqs. 2.25 and 2.26). For a horizontally uniform and vertically decaying breaker impulse, the wave-induced terms can be specified approximately as (Rascle et al., 2012):

$$\mathbf{F}(z) = \int_c \mathcal{M}_b(z, c, \vartheta) \mathcal{P}(c) dc, \quad \text{and} \quad P^{wb}(z) = \int_c \varepsilon_b(z, c, \vartheta) \mathcal{P}(c) dc, \quad (3.2)$$

where the frictional acceleration \mathbf{F} has been introduced in Eq. (2.1), ϑ is the angle between wind and wave directions, and the Probability Density Function (PDF), $\mathcal{P}(c)$, corresponding to speed c is expressed as

$$\mathcal{P}(c) = \frac{\alpha_b g \Lambda(c)}{2\pi c^2}.$$

Alternatively, Tian et al. (2010) obtained an expression for the wave breaking energy loss, P^{wb} , by the means of a breaking-induced eddy viscosity model.

Craig and Banner (1994) and Craig (1996) made a numerical investigation of near-surface turbulence under the effects of wave breaking using a wave-modified MY closure. Noh et al. (2004) reported the importance of including wave breaking effects to predict efficiently the formation of a diurnal or seasonal thermocline under a stabilizing heat flux. Gemmrich and Farmer (1999) modified the Craig and Banner (1994) model by including the LC effects, and found very good agreement between model and observation near the sea surface by assuming a constant water-side roughness length. Recently, several studies have incorporated wave effects on upper ocean mixed layer dynamics; for example, D'Alessio et al. (1998) and Burchard (2001) for the effects of wave breaking, Stips et al. (2005) and Jones and Monismith (2007) for the surface roughness parametrization, and D'Alessio et al. (1998), McWilliams et al. (1997), Kantha and Clayson (2004), and Harcourt (2013) for the effects of LC. Despite great efforts, proper parameterizations of these wave-induced processes are still under debate.

Generally, numerical methodologies for studying wave effects on the upper ocean mixing can be split into Direct Numerical Simulation (DNS), Large Eddy Simulation

(LES), and Reynolds Averaging Navier Stokes (RANS) techniques. DNS based models give a comprehensive description of flow quantities since they resolve all turbulent scales. They therefore require a very small spatial separation of sampling points resulting in very large number of grid points ($\sim Re^{9/4}$, where Re denotes the Reynolds number). Due to large Reynolds numbers which occur in geophysical processes, which will require the use of massive computational resources, DNS cannot be used as a desirable method for geophysical applications. RANS and LES are then alternative techniques to DNS, based on resolving the unresolved motions by means of stress closure techniques (Tejada-Martinez et al., 2012). As discussed in Section 2.3.2, the properties of the closure models play a significant role in the accuracy of the predicted mean flow quantities, especially in the presence of surface gravity waves. However, in the LES model in which the corresponding closure (Subgrid Scale (SGS)) needs to account for the effects of eddies with sizes smaller than the simulation grid size (Sullivan et al., 2012). I explain briefly here how the LES technique is derived in the presence of surface gravity waves.

A LES model is based on scale separation between large energetic (resolved) eddies and small (unresolved) dissipative eddies, and uses a low-pass filter in wavenumber space. This low-pass filter damps out scales smaller than the size of the filter width, Δ . Applying the spatial filtering operation to wave-phase averaged equation (2.15) which includes CSF and Craik-Lobovich vortex forcing, results in the LES governing equations for the wave-modified momentum:

$$\begin{aligned} \frac{\partial \bar{u}_i}{\partial t} + u_j \frac{\partial \bar{u}_i}{\partial x_j} + \varepsilon_{ijk} f_j (\bar{u}_k + u_k^i) &= -\frac{1}{\rho_0} \frac{\partial \bar{\Pi}}{\partial x_i} + g \delta_{3i} \frac{\rho}{\rho_0} \\ &= \varepsilon_{ijk} u_j^s \bar{\omega}_k + F_i + \frac{\partial \tau_{ij}^{sgs}}{\partial x_j}, \end{aligned} \quad (3.3)$$

where F_i is a forcing term, here representing the generation of small-scale wave breaking induced momentum, the overbars denote the application of the low-pass filter, and the SGS stress, τ_{ij}^{sgs} , is defined as

$$\tau_{ij}^{sgs} = \bar{u}_i \bar{u}_j - \overline{u_i u_j}. \quad (3.4)$$

These stresses represent the influence of the smaller unresolved scales on the resolved energetic scales. This equation also shows a closure problem because the second term on the RHS requires knowledge of the unfiltered velocity field. Typically, the SGS stresses are decomposed into dilatational, $\delta_{ij} \tau_{kk}^{sgs}/3$, and deviatoric, τ_{ij}^{sgsd} , parts, as follows:

$$\tau_{ij}^{sgs} = \tau_{ij}^{sgsd} + \delta_{ij} \frac{\tau_{kk}^{sgs}}{3}.$$

The deviatoric part can be parameterized via the Smagorinsky closure as

$$\tau_{ij}^{sgsd} = -2\nu_t^{les} \bar{S}_{ij}, \quad (3.5)$$

where $\nu_t^{les} = (C_s \bar{\Delta})^2 |\bar{S}|$ is the LES eddy viscosity, C_s is the Smagorinsky coefficient, and $S_{ij} = (\partial u_i / \partial x_j + \partial u_j / \partial x_i) / 2$ and $|\bar{S}| = (2\bar{S}_{ij} \bar{S}_{ij})^{1/2}$ are the filtered strain rate, and its norm, respectively. To extend the Reynolds stress parametrization (Eq. 3.5), the

Reynolds stresses of less energetic unresolved eddies subject to wave effects are determined prognostically using a LES-Reynolds decomposition technique. In this approach, the filtered variables are decomposed into the mean resolved, $\{\bar{u}_i\}$, and the resolved velocity fluctuation, \bar{u}'_i , where $\{\cdot\}$ denotes the Reynolds averaging operation. Applying this decomposition to Eq. (3.3) together with other manipulations lead to transport equations for the Reynolds stresses and TKE, respectively. For the sake of brevity, I only present the viscous dissipation and SGS dissipation rates, which can be written as:

$$\varepsilon_{ij} = -2 \left\{ \frac{\partial \bar{u}'_i}{\partial x_k} \frac{\partial \bar{u}'_j}{\partial x_k} \right\} \quad \text{and} \quad \varepsilon_{ij}^{sgd} = \left\{ \tau_{ik}^{sgsd} \frac{\partial \bar{u}'_j}{\partial x_k} \right\} - \left\{ \tau_{jk}^{sgsd} \frac{\partial \bar{u}'_i}{\partial x_k} \right\}.$$

For more detailed information, the reader is referred to Tejada-Martinez et al. (2012).

3.2 Wave-modified models

Upper ocean mixing parameterizations and models exhibit substantial biases in predicted flow quantities in the presence of surface gravity waves. These models traditionally use atmospheric forcing and subsurface profiles of tracers (salinity and temperature) and velocity to predict upper ocean turbulent fluxes and other quantities. A collection of such models has been implemented in the GOTM model system in very general and modular manner. An important feature of these models however is that they assume the sea surface as a solid boundary and exclude wave effects in momentum transfer and the injection of energy into the water column. To better identify the essential processes affecting the turbulence mixing near the sea surface, it is required to develop, diagnostically and prognostically, the wave effects which are ignored in classical modeling approaches. An overview of some one-dimensional vertical water-column studies including surface gravity wave effects is listed in Table 3.1.

Table 3.1: Table of one-dimensional vertical mixing models which include the following processes: Wave Breaking (WB), here we treat WB as both a surface source for TKE and a volume source of energy; non-breaking wave (NBW), we used these parameterizations in our **Papers IV and V**; Coriolis-Stokes forcing (CSF), the CSF used in **Papers I, IV, and V**; and Langmuir Turbulence (LT), LT employed in **Papers IV and V**.

Reference	WB	NBW	CSF	LT
Craig (1996); Craig and Banner (1994)	Y	N	N	N
Terray et al. (1996)	Y	N	N	N
Burchard (2001)	Y	N	N	N
Kantha and Clayson (2004)	Y	N	Y	Y
Raschle et al. (2007)	Y	N	Y	N
Mellor (2013)	Y	N	N	N
Jenkins et al. (2012)	Y	Y	Y	Y
Huang et al. (2011)	Y	Y	N	N
Janssen (2012)	Y	N	Y	Y

3.3 Observational methods

Processes such as wind-driven currents, wave breaking, air bubble entrainment, acoustic noise, and LC significantly contaminate turbulent quantities measured near the moving interface. Typical difficulties that are potentially important can be divided into the following incomplete list: 1) instrumental errors; 2) carrier platform motion; 3) geometry of the platform, sensors, and neighboring structures; 4) aliasing (the tradeoff between accuracy and resolution); 5) vibration; and 6) overlapped wave and turbulence scales. Turbulence measurements may further require intensive time (labour), frequent instrument calibration and maintenance, a high level of user interaction, and intensive and complicated post-processing. Thus, any errors in implementing aforementioned requirements may also make estimations of turbulence statistics erroneous.

Eddy Covariance Technique (ECT) is a successful and the most accurate direct approach for measurement of turbulent fluxes (Edson et al., 1998). Although ECT delivers accurate and comprehensive information on episodic and intermittent turbulence, such direct measurements of turbulence are rare and difficult in the upper ocean, particularly in the presence of non-turbulent wave motions (Fujitani, 1981; Pedreros et al., 2003). Consequently, indirect methods are commonly employed to study upper ocean turbulence depending on the choice of sensors, measurement techniques, the degree of sophistication of the data processing, and intensity and duration of data collection. Typical indirect observations of turbulence in the ocean upper layer are carried out using microstructure profilers equipped with shear probes and/or thermistors, hot-wire and hot-film anemometers, particle-image velocimeters (PIVs), laser Doppler velocimeters (LDVs), acoustic Doppler velocimetry (ADV), and high frequency acoustic Doppler current profilers (ADCP). To overcome the problem of sampling rate in indirect techniques and due to inability of most of available instruments to satisfy the required spatial resolutions, additional assumptions have to be employed. For example, to extract ε using ADV, ADCP, and microstructure shear probe signals, the frozen turbulence hypothesis (Taylor's hypothesis) needs to be invoked, using a mean translational speed. However, in the presence of wave effects, wave-turbulence interaction can lead to the frozen turbulence hypothesis becoming invalid and turbulent eddies move by combined wave orbital velocities and mean currents (Lumley and Terray, 1983). This unsteady advection creates a frequency shift in the measured velocity spectra that influence the quality of separation of waves from turbulent motions, specially in using inertial subrange based techniques (to identify ε from the velocity spectra). PIV and the pulse-to-pulse coherent unidirectional Doppler profiler, among others, are able to collect velocity signals with no need to consider the Taylor frozen turbulence hypothesis. Because the (horizontal) velocity wavenumber spectrum is directly resolved by these instruments.

In general, however, turbulence observations are restricted to measure TKE dissipation rate. Measurements of ε near the sea surface in the laboratory, ocean, and lakes show in many cases that turbulence and its associated mixing are enhanced in the presence of surface gravity waves. In a water tank experiment using an oscillating grid just below the surface, Thompson and Turner (1975) showed that dissipation decays with depth with a power -4 with respect to the distance below the grid (which is conceived as breaking surface mechanism). Agrawal et al. (1992) and Kitaigorodskii and Lumley (1983) performed field measurements on Lake Ontario from a fixed tower, and reported

that the turbulent boundary layer in the UOBL depends on the growth of wind generated waves, with values of ε beneath the wavy interface greater than those predicted by the LOW. Thorpe and Humphries (1980) and Thorpe and Hall (1983) experiments at the California shelf suggested that wave breaking injects energy into the water column associated with a reduced velocity gradient below the surface over a depth approximately 0.2 times the surface wavelength. They also suggested that the logarithmic wall analogy is no longer valid near the wavy surface. Osborn et al. (1992) conducted a short-time experiment using an uplooking acoustic instrument together with shear probes mounted on a submarine in the Pacific Ocean. They found enhancement of ε consistent with those observed by Thorpe and Hall (1983), Kitaigorodskii and Lumley (1983), and Kitaigorodskii et al. (1983). Using an ascending vertical profiler in the Pacific Ocean, Anis and Moum (1995) reported enhanced dissipation rates with an exponential decay near the sea surface under surface waves. While the aforementioned studies show enhanced TKE near the sea surface under the influence of wave forcing, some other studies have proposed a general agreement between ε and LOW. Churchill and Csanady (1983) noted that near surface measurements of turbulence show agreement with LOW analogy. Jones (1985) measured velocity under strong wind forcing in the Bass Strait. He concluded that the measured ε can be scaled appropriately by the wall scaling. Cheung and Street (1988) measured turbulence in a laboratory experiment with a range of wave conditions. They found that the behaviour of the turbulent velocity was similar to that observed near rigid walls. However, in some cases in their experiment with wind-ruffled, mechanically generated waves in a tank, they reported increased levels of turbulence away from the surface, and concluded that in those cases waves are not perfectly irrotational, with a non-zero phase difference between \tilde{u} and \tilde{w} , where \tilde{u} and \tilde{w} are the horizontal and vertical components of the wave orbital velocity. Recently, Sutherland et al. (2013) conducted a series of field experiments in the North Atlantic using an upwardly free-rising air-sea interaction Profiler. Their measured ε show surprisingly better fit with those predicted by LOW. Thus, existing observational evidence shows that turbulence below wind waves may and may not obey LOW scaling.

Chapter 4

The present study

4.1 Objectives and approaches

Surface waves, as a widespread phenomenon covering all the world oceans, interact in very complex nonlinear ways with marine structures, and provide a mechanism for the exchange of momentum, heat, gas, energy, and moisture across the air-sea interface. In spite of difficulties in making necessary field measurements, wave interaction with physical processes in the upper ocean has been subject to many theoretical, laboratory, observational, and numerical studies during the last four decades. Recent research has shown that both wave breaking and swell waves are able to influence the structure of the turbulence in the lower marine atmospheric boundary layer and thus to affect load and fatigue of turbine rotor blades. In addition, wave breaking will increase loads exerted on turbine foundations and monopile structures. Investigation of wave processes is very necessary for the development of offshore wind farms, especially in deep water, and for quantifying the active air-sea exchange processes. To achieve the objectives of this PhD thesis defined in Chapter 1, we investigate wave-current and wave-turbulence interactions as one of important upper ocean mixing-related issues numerically and experimentally.

The specific objectives of this PhD project can be summarized as: 1) obtaining long-term oceanic measurements of TKE dissipation rates near the sea surface; 2) quantifying observationally the influence of the surface waves in the collected data set for ϵ ; and 3) obtaining further understanding of the coupled processes by improving and modifying a one (vertical) dimensional mixing model by including wave effects.

To approach these objectives and particularly those mentioned in Chapter 1, we employ an instrument (Section 4.3.1) equipped with the required oceanographic sensors, and develop the required data analysis techniques, such as data correction and screening, to satisfy the measurement goals. Furthermore, we investigate wave-induced mixing parametrization techniques using appropriate closure methods in the GOTM model.

4.2 Numerical tools

To improve air-sea model forecasts in the presence of gravity waves, we target on understanding the essential processes, improving parameterizations, and checking the wave-modified model performance. Our approaches are based on 1) understanding

the physical processes such as Stokes drift, breaking and non-breaking waves, and LC mechanisms and their interactions with upper ocean current and turbulence; 2) calculating the wave-modified scaling in a one-dimensional vertical mixing model; 3) performing simulations for the various forcing conditions and evaluating the reliability of the numerical results through model-observation intercomparisons with the measured ε (and from some other published data sets in literature). All listed modifications have been implemented in the GOTM model, and communication with the wave field is by means of an input data file as the temporal evolution of wave energy spectrum. Based on this input wave data, the wave-induced terms (for example S_{in} and S_{ds}) are estimated internally in the corresponding developed wave module (Fig. 4.2). The modifications have been performed in such a way that the user can easily switch between different parameterizations and modifications, and the toolbox can be developed further to include new features by both modellers and observationalists. More information on the coupling methodologies and theories used can be found in **Papers I, IV, and V**.

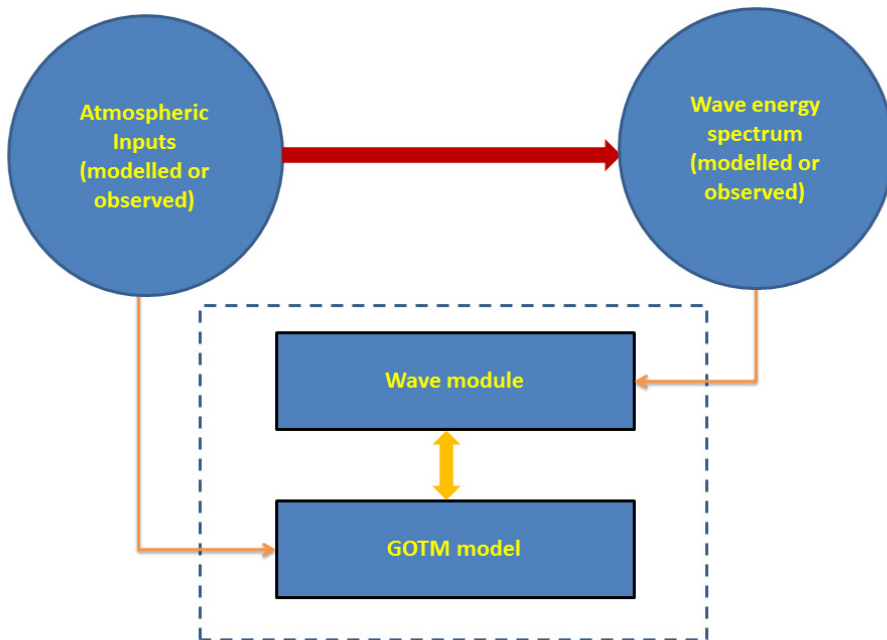


Figure 4.1: Exchange of variables between wind, the wave module, and GOTM. For the coupling of waves with GOTM, the Coriolis-Stokes forcing, wave-induced momentum, wave breaking production, Stokes shear production, non-breaking parameterizations are computed internally in the wave module, using data from wave energy spectrum input file. The wave energy spectrum is calculated using an empirical formulation if the wave energy information is not available.

4.2.1 Data processing and reduction

In this section, I describe some post-processing procedures which have been used in **Papers II-VI** to remove or reduce the effects of the motion and geometry of carrier platforms from measurements collected from high-resolution velocity, pressure transducer, and shear probes.

Motion correction

In this section, I focus on the motion-correction algorithm applied to the velocity field contaminated by the translational and angular velocities and instantaneous tilt of a specialized sensor (ADV or sonic anemometer). Two reference frames are specified: 1) the right-handed coordinate system with x , y , and z axes pointing outward to the nose, the right-hand side, and the top of the carrier platform, respectively. Three angular coordinates are defined, corresponding to motions about the x , y , and z axes, respectively: roll, ϕ , positive when the port-side goes up; pitch, θ'' , positive when the nose goes down; and heading, ψ , positive when the platform rotates counterclockwise when viewed from above; and 2) a non-rotating fixed frame of reference with axes pointing out to north, east, and upward, respectively (**Papers II and VI**).

Orientation of the specialized sensor is determined using a 3-axis accelerometer, a 3-axis angular rate gyroscope, and a 3-axis magnetometer signals from Inertial Motion Unit (IMU) mounted on the platform. These orientations can be obtained precisely from the gravitational components of accelerometer signals if the body acceleration is negligible compared with the acceleration due to the gravity. Integrating gyroscope data leads to an accurate estimate of orientation when sampling is carried out on a short-time duration, and the accuracy of magnetometer for the purpose of calculating the platform heading is strongly dependent on the amount of magnetic disturbance present. To improve the estimate of platform orientation, the motion package signals are combined together by means of a complementary filtering in which the sum of two corresponding filter transfer functions is unity for the whole frequency range. Accelerometer signals give a reasonably accurate estimate of orientation at low frequencies and a noisy estimate at high frequencies. Platform orientation from the gyroscope signal can be achieved more accurately at high frequencies than at low frequencies. Combining the long-time, accurate accelerometer signal with the short-time, accurate gyroscope signal will then give a more accurate estimate of pitch and roll. We use a fourth-order Butterworth filter backward and forward for both low-passed and high-passed filters, to avoid phase change. The pitch and roll data obtained are then used to rotate the magnetometer data to the horizontal plane. The low-pass filtered and rotated magnetometer data give a good estimate of the platform heading at low frequencies, and can be combined with heading data extracted from the gyroscope signals to produce an accurate estimate of the platform heading at all frequencies. Using calculated platform Euler angles (**Paper VI**), the specialized sensor motion in its body frame is expressed as

$$\mathbf{V}_{mot} = \mathbf{V}_{trans} + \mathbf{V}_{rot} = \mathbf{V}_{trans} + \boldsymbol{\Omega}_{obs} \times \mathbf{R}, \quad (4.1)$$

where \mathbf{V}_{mot} is the platform body velocity, $\boldsymbol{\Omega}_{obs}$ is the angular rotation vector relative to the body frame, \mathbf{R} is the position vector of the motion package with respect to the sensor, and \mathbf{V}_{trans} and \mathbf{V}_{rot} are translational and rotational velocities of the sensor, respec-

tively. To calculate \mathbf{V}_{trans} using pitch and roll, we remove the gravitational acceleration from the measured acceleration signals:

$$\ddot{\mathbf{x}}_{obs} = \begin{bmatrix} a_x \\ a_y \\ a_z \end{bmatrix} + \begin{bmatrix} -g \sin(\theta'') \\ g \sin(\phi) \cos(\theta'') \\ g \cos(\phi) \cos(\theta'') \end{bmatrix}, \quad (4.2)$$

where $\ddot{\mathbf{x}}_{obs}$ is the body acceleration signal, which is used to estimate the translational velocity by

$$V_{trans} = \int_t \tilde{\ddot{\mathbf{x}}}_{obs} dt,$$

where $\tilde{\ddot{\mathbf{x}}}_{obs}$ is obtained by applying the high-pass filter to $\ddot{\mathbf{x}}_{obs}$, in order to remove inherent accelerometer drift (Edson et al., 1998). The wave-induced platform motion contamination can be removed from the observed velocity in the reference frame by

$$\mathbf{V}_{true} = \mathbf{T}[\mathbf{V}_{obs} + \mathbf{V}_{mot}], \quad (4.3)$$

where \mathbf{V}_{obs} is the flow velocity measured by the ADV or sonic anemometer, and \mathbf{T} is the coordinate transformation from the body frame to the earth frame. The coordinate transformation matrix is obtained by multiplying three rotation matrices calculated from the Euler angles. The order of rotation matrices multiplications results in different transformations, and for very small rotation increments, the sensitivity of transformation reduces with respect to multiplication order. In this study, I use the sequence $\psi \rightarrow \theta'' \rightarrow \phi$. Thus, \mathbf{T} is expressed in the right-handed coordinate system as

$$\begin{aligned} \mathbf{T} &= \begin{bmatrix} \cos(\psi) & -\sin(\psi) & 0 \\ \sin(\psi) & \cos(\psi) & 0 \\ 0 & 0 & 1 \end{bmatrix} \begin{bmatrix} \cos(\theta'') & 0 & \sin(\theta'') \\ 0 & 1 & 0 \\ -\sin(\theta'') & 0 & \cos(\theta'') \end{bmatrix} \begin{bmatrix} 1 & 0 & 0 \\ 0 & \cos(\phi) & -\sin(\phi) \\ 0 & \sin(\phi) & \cos(\phi) \end{bmatrix} \\ &= \mathbf{T}(\psi)\mathbf{T}(\theta'')\mathbf{T}(\phi). \end{aligned} \quad (4.4)$$

The angular velocity vector is determined for a right-handed coordinate system in the body frame by the following ordinary differential equation:

$$\boldsymbol{\Omega}_{true} = \begin{bmatrix} \dot{\phi} \cos(\psi_{obs}) \cos(\theta''_{obs}) + \dot{\theta}'' \sin(\psi_{obs}) \\ \dot{\theta}'' \cos(\psi_{obs}) - \dot{\phi} \sin(\psi_{obs}) \cos(\theta''_{obs}) \\ -\dot{\psi} - \dot{\phi} \sin(\theta''_{obs}) \end{bmatrix},$$

where the overdot denotes the time derivative of the Euler angles, and $\boldsymbol{\Omega}_{true} = [\dot{\phi}, \dot{\theta}'', \dot{\psi}]^T$ used in Eq. (4.3).

Flow distortion

Flow distortion can significantly corrupt turbulence measurements because of the generation of secondary motions in the vicinity of carrier platforms, sensors, and other neighboring objects. Generally, the flow distortion problem can be approximately solved in the vicinity of a body of revolution, either computationally or analytically, using potential flow theory for simplified bodies (**Paper II**).

Using potential flow theory, Oost et al. (1994) examined several methods for correcting of turbulent fluxes in the atmospheric boundary layer. They concluded that the

corrections are strongly dependent on the shape of the object (carrier platforms) and the distance of the sensors from the object. Their proposed models were applied to three sets of data suggesting that the usual form of tilt correction is not sufficient to correct for flow disturbances surrounding the supporting platforms. Dupuis et al. (2003) measured the momentum and heat fluxes obtained from the R/V L'Atalante, a spar buoy, and from aircraft, in a fetch-limited situation using the inertial-dissipation method to calculate fluxes. To include the flow distortion contribution, they performed numerical simulations of flow distortion caused by the ship. Their results for the mean wind speed showed that the distortion effects vary significantly as a function of wind speed and direction, with an enhancement when the relative difference between the flow direction and the bow is greater than 30° .

Here, I will present briefly how to calculate the secondary distorted flow around the objects with shapes similar to MATS. To apply the potential flow assumption using analytical methods, I approximate the object shape as a prolate spheroid. It is useful to transform the Cartesian body coordinate system (x, y, z) to a prolate spheroid coordinate system (ξ, μ, ϖ) using the following relations (Lamb, 1932):

$$\begin{aligned} x &= a\mu\xi, \\ y &= a\sqrt{1-\mu^2}\sqrt{\xi^2-1}\cos(\varpi), \\ z &= a\sqrt{1-\mu^2}\sqrt{\xi^2-1}\sin(\varpi), \end{aligned}$$

where the foci of spheroid coordinates are at $x = \pm a$. Without loss of generality, I assume that the prolate spheroid coordinate system has major axis, b , along the x -axis of MATS and minor axis, c , along the z axis, and its surface satisfies $\xi = \xi_0$ where $\xi_0 = b/a$, and $a = b\sqrt{1-c^2/b^2}$. For the inviscid, irrotational fluid, the velocity field can be expressed as the gradient of a scalar potential function Φ which can be compactly expressed by

$$\Phi = \Phi(x, y, z, \xi).$$

Using Φ and assuming that the body of revolution moves with uniform velocities in the x , y , and z directions, the translational distorted velocity tensor A^{fd} is obtained. Similarly, in the case of rotations about the x , y , and z axes, the rotational tensor B^{fd} is then calculated. According to Lamb (1932), this distorted flow can be represented as a linear combination of platform relative (linear) velocity and angular velocity. These matrices are then combined with Eq. (4.3) to remove distortion effects, using potential theory.

Wave estimate

In this section, I describe how to estimate the true wave information by combining signals from a pressure sensor and a motion package. Both instruments have been mounted on MATS, and the wave energy spectrum is calculated through a multistep procedure as presented in **Paper V**.

The dynamic pressure is estimated for the deep water using linear small-amplitude wave theory as

$$p^d(z, t) = \rho_w g e^{-kz} \eta, \quad (4.5)$$

where $k = 2\pi/\lambda$ is the wavenumber, λ being the wavelength. To avoid strong noise growth caused by depth-attenuation of the pressure signal, I apply a cut-off frequency,

f_{cut} , and extrapolate the wave energy spectrum beyond f_{cut} by f^{-5} (**Paper I**). The contaminations induced by platform motion are removed, using the mounted accelerometer and the gyroscope angular rate signals. The accelerometer and gyroscope contributions in the estimation of surface gravity waves can be computed using the vertical acceleration, pitch, and roll data. Let $\ddot{\mathbf{x}}_{obs}$ again denotes the observed accelerometer signal in the rotating frame. The vertical acceleration in the reference coordinate system (the non-rotating frame) is then calculated by

$$\ddot{z}_{acc} = [\mathbf{T}(\phi, \theta'', \psi) \ddot{\mathbf{x}}_{obs}] \cdot \hat{z}, \quad (4.6)$$

where \mathbf{T} is given by Eq. (4.4). The vertical acceleration \ddot{z}_{acc} is then twice integrated, and the inherent accelerometer measurement noise in is filtered prior to each integration. The platform vertical displacement can then be computed by

$$\eta^{acc} = \int \int \ddot{z}_{acc} dt' d\tau', \quad (4.7)$$

where τ and t' are elapsed times. The tilt height of the pressure sensor is calculated using the rotational angles and the vector distance from the motion package to the pressure sensor, \mathbf{R} , as

$$\eta^{tilt} = [\mathbf{T}(\phi, \theta'', \psi) \mathbf{R}] \cdot \hat{z}. \quad (4.8)$$

To conclude, we combine the displacements, together with the raw pressure signal in frequency space, and using Eq. (4.5) to estimate the wave energy spectrum. It should be noted that we used only the vertical acceleration information to correct the pressure signal in **Paper V**.

Dissipation rate of TKE from shear probes

The average turbulence energy dissipation rate based on local isotropy is given by

$$\varepsilon = \nu \overline{\left(\frac{\partial u'_i}{\partial x_j} + \frac{\partial u'_j}{\partial x_i} \right) \frac{\partial u'_j}{\partial x_i}}, \quad (4.9)$$

where ν is the kinematic viscosity, and the overbar denotes a time average. By assuming local isotropy of turbulence, the one-dimensional dissipation rate measured from vertical gradient profiles of the horizontal current fluctuations is given by (Taylor, 1935):

$$\varepsilon = 15\nu \overline{\left(\frac{\partial u'_1}{\partial x_1} \right)^2} = \frac{15}{2} \nu \overline{\left(\frac{\partial u'_1}{\partial x_3} \right)^2}, \quad [\text{W kg}^{-1}]. \quad (4.10)$$

In this study, the small-scale shear $\partial u' / \partial z$ is measured using two shear probes mounted on both MATS and a vertical microstructure profiler. After suppressing the low frequency vibration disturbances of the vessel using accelerometer signals (Goodman et al., 2006), the dissipation rate is obtained from the measured shear spectra:

$$\varepsilon = \frac{15}{2} \nu \int \Psi_{shear}(k) dk, \quad (4.11)$$

where Ψ_{shear} is the measured shear probe spectrum after conversion from frequency to wavenumber spectrum via Taylor's hypothesis. Applying the Taylor's hypothesis for the vertical microstructure profiler depends on the fall velocity of the instrument, and for the MATS shear signals depends on the flow past the sensor (**Papers II, III, and IV**).

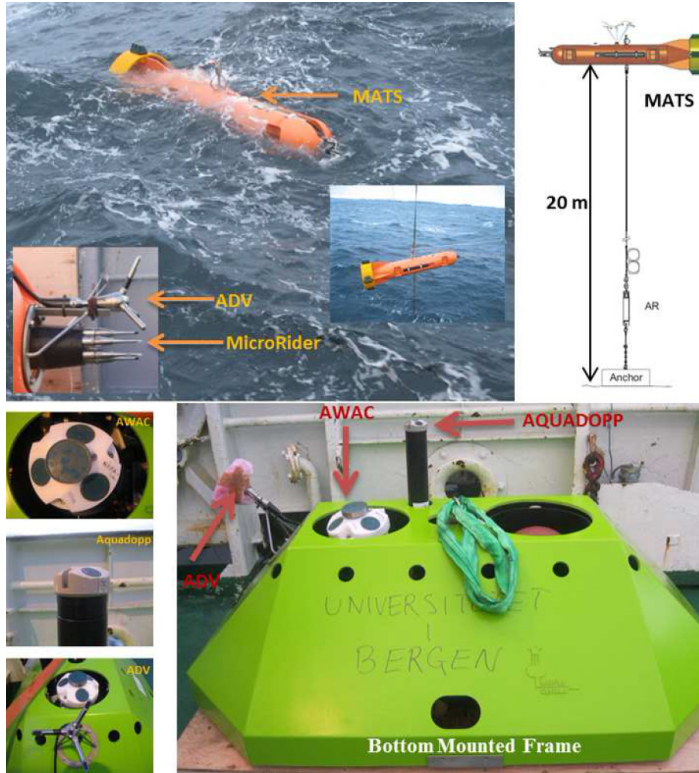


Figure 4.2: (Top) MATS deployment and the different components, and (Bottom) Bottom mounted frame with the installed oceanographic sensors.

4.3 Instruments and field works

4.3.1 MATS

The Microstructure Autonomous Turbulence System (MATS) has been designed to collect microstructure time series of near-surface turbulence at a fixed level. The platform is a low-drag buoy, custom modified by Flotation Technologies to fit the turbulence instruments. The buoy is equipped with a MicroRider turbulence instrument package consisting of two air-foil shear probes, two fast response thermistors, a pressure transducer, a two-axis vibration sensor, a precision pitch and roll sensor, and a three-axis magnetometer. Additionally, a low-power 6-axis motion sensor (Inertial Motion Unit (IMU)) is fitted into the MicroRider. A three-component ADV, Nortek Vector, is interfaced with the MicroRider. The sensor head of the Vector is rigidly fixed to the buoy. The entire system is powered by two rechargeable lithium-ion battery packs, giving an estimated operating time of 500 h. With a 25% duty cycle, this instrument can sample 20 GB of data for about 85 days. The buoy is the upper element of a bottom-anchored mooring line, allowed to align with the current, and is set to acquire data in the upper 5–10 m. The system allows for measurements using two independent methods,

sampling different parts of the turbulence spectrum: eddy correlation measurements of turbulent momentum and heat flux sampled in the energy-containing and near-inertial subranges, and dissipation rate measurements in the dissipation subrange (**Papers II and VI**).

It should be noted that the temperature gradient spectrum cannot be resolved efficiently, and velocity spectra calculated from ADV signals are severely noisy, so that the inertial subrange is either very narrow or not detectable in most cases. Hence, the performance of the motion correction algorithms presented in the previous section are evaluated by applying them to the high resolution sonic anemometer data (**Papers VI**).

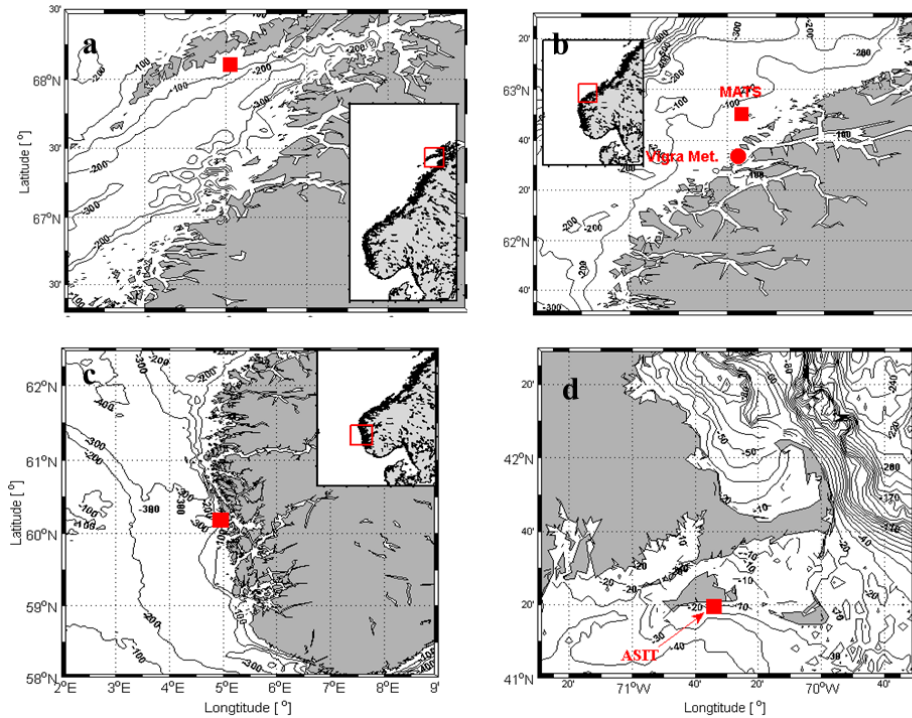


Figure 4.3: Maps showing cruise areas where all instruments were deployed: a) Vestfjorden, northern Norway (8–13 April, 2011); b) Havsul area (end of October 2011 to end of January 2012); c) Marstein (28–30 November 2012; and 30 November 2013 to 5 December 2013); and d) Martha’s Vineyard, Massachusetts, USA, (13 April to 29 June 2010).

4.3.2 Experiments

Vestfjorden, 2011

Surface wave, current, and turbulence data were collected during the BIOWAVE-OILWAVE cruise in Vestfjorden, Lofoten, northern Norway on 8–13 April 2011 (Fig. 4.3-a). Three different moorings were deployed during the cruise with distance

approximately 2 km apart from each other forming a triangle. The first mooring contained two ADCPs, the second was the Waverider buoy, and the third was MATS equipped with a number of oceanographic sensors (**Paper II**). MATS was deployed at depth of approximately 128 m and fixed about 12 m below the sea surface.

Havsul, 2012

Observations of ocean turbulence, background currents, hydrography, and surface waves were carried out during a cruise of the Research Vessel (R/V) Håkon Mosby. The measurement site was approximately 6 km offshore of the Havsul-I area off the west coast of Norway, the first site in Norway with a concession for an offshore wind park (Fig. 4.3-b). Near-surface turbulence was sampled using both MATS and a free-falling profiler (MSS) for a period between 25 and 31 October 2011. The atmospheric data were logged from the ship's meteorological mast at a height of 15 m. A Fugro-Oceanor WaveScan buoy and an oceanographic mooring were also deployed during this cruise. The water depth at the measurement site is approximately 130 m. MATS and the mooring were recovered on 10 January 2012 and 6 March 2012, respectively (**Papers IV and V**).

Marstein, 2012 and 2013

Ocean currents, surface gravity waves, dissipation rates of TKE, and atmospheric turbulent fluxes were measured during two short cruises of the R/V Håkon Mosby in December 2012 and November 2013, respectively. The measurement site was approximately 30 km southwest of Bergen at 20 m water depth. The deployment site is less than 5 km east of the 200 m isobath of the Norwegian trench (Fig. 4.3-c). Measurement of air-sea interaction processes in both above and below the air-sea interface were carried out from floating platforms including ship, buoys, MATS (fixed at 10 m below the surface), and a Bottom Mounted Frame (BMF) structure (Fig. 4.2). To keep track of the locations and attitudes of platforms, all structures except BMF were equipped with an IMU system. The BMF was equipped with an AWAC (Acoustic Wave and Current Profiler), an uplooking Aquadopp, and an ADV with a horizontal plate and a 45° slanted bracket (Fig. 4.2). The AWAC performs dual measurements of both ocean currents and surface gravity waves from a single fixed installation. The upward-looking Aquadopp provided background current measurements. In contrast to the MATS, installation of the ADV on the BMF enabled us to record high-resolution flow and turbulent flux measurements without any need for motion correction. In a similar way to the MATS, the ADV collected samples during 15 minute bursts per hour (**Paper III**).

Martha's Vineyard Coastal Observatory, 2010

Measurements of turbulent fluxes in the marine atmospheric boundary layer were performed using the Air Sea Interaction Tower (ASIT) at the Martha's Vineyard Coastal Observatory, Massachusetts, USA, and from a moored floating buoy in the vicinity of ASIT between 13 April and 29 June, 2010 (Fig. 4.3-d). Both ASIT and the buoy were equipped with a direct covariance flux system and an inertial motion unit to measure turbulent fluxes at low wind speeds (**Paper VI**).

Chapter 5

Introduction to the papers

Although the general impact of waves on the hydrodynamics covers a broad range of disciplines, from turbulence closure to nearshore circulation, the papers listed here have concentrated on some specific aspects of wave-current and wave-turbulence interaction. Generally, the context of the papers can be divided into three parts: 1) wave-current-turbulence interaction including coupling methodologies, modifications, and implementations; 2) signal processing and data analysis techniques; and 3) instrumentation and turbulence sensor specifications. Here, I present the description for each paper separately in the order introduced in the Section *Outline with list of papers*.

Paper I. Surface gravity wave effects on the upper ocean boundary layer: modification of a one-dimensional vertical mixing model

1. *investigate coupling methodology based on wave-induced terms derived from a second-order perturbation expansion of the Navier-Stokes equations in Lagrangian coordinates.*
2. *study the roles of Coriolis-Stokes forcing and wave breaking momentum terms in the dynamics of upper ocean currents and turbulence.*

In this paper, we investigate the effects of surface gravity waves on upper ocean currents and turbulence based on Jenkins (1987) and Jenkins (1989) formulations by the use of Coriolis-Stokes forcing and wave-current interaction momentum transfer terms. For numerical study, we modify the one-dimensional General Ocean Turbulence Model (GOTM). Moreover, we illustrate how such modifications influence the prediction of upper ocean currents and turbulence using some existing data sets. Results suggest that inclusion of Stokes drift increases the magnitude of the wind-induced surface currents by about 35% and its veering by about 30%. Furthermore, wave-induced momentum reduces the surface current slightly, and has a trivial impact on its veering. Additionally, we provide a simple finite element numerical solver for the numerical study of steady-state wave-modified Ekman currents.

Paper II. Autonomous ocean turbulence measurements using shear probes on a moored instrument

1. *introduce MATS and its components, coordinate system, and sampling information in detail.*

2. *provide the required data processing techniques that should be accounted in such measurements from mobile systems, including platform motion correction, shear probe data processing concerns in the presence of surface waves, platform angle of attack effects, and data quality control criteria.*
3. *test the ability of MATS to estimate gravity waves and dissipation rates of TKE by deploying MATS in Vestfjorden in Northern Norway (April 2011) in a 4-day campaign.*

In this paper, skill of a newly designed MATS is tested in a short-term deployment to measure upper ocean turbulence. Although the platform was designed to measure ϵ in two different parts of turbulent energy wavenumber spectrum, it was found impossible to apply the Eddy Covariance Technique (ECT) using ADV measurements, mainly as a result of severe contamination of velocity spectra in the inertial subrange. In addition, the temperature gradient measurements could not be resolved adequately in the dissipative subrange, and only the shear spectra have nearly less contamination in the frequency range 1–20 Hz. The values of ϵ estimated using shear spectra are consistent with the scaling expected from wave breaking.

Paper III. Turbulence measurements in shallow water from a subsurface moored moving platform

1. *deploy MATS in shallow water together with a bottom mounted platform as a reference fixed platform for measurement of both waves and turbulence.*
2. *test the ability of MATS to measure ϵ successfully in the presence of both surface gravity waves and bottom topography. Preliminary results suggest that observed dissipation rates of TKE are consistent with the expected scaling from breaking waves.*

In a joint atmospheric-oceanic field campaign in December 2012, the performance of deployed systems was evaluated in a water depth of approximately 20 m. This experimental setup contains MATS, a bottom frame platform (equipped with an ADV, a Nortek AWAC, and an upward looking current profiler), and a Direct Covariance Flux (DCF) system mounted on mobile vessels at the front bow of RV Håkon Mosby ship, and a floating buoy, instrumented to measure atmospheric marine boundary layer turbulence characteristics. In this experiment, all deployed instruments experienced such harsh weather conditions, that the floating buoy capsized during the deployment.

Paper IV. Turbulence structure in the upper ocean: a comparative study of observations and modelling

1. *present observations of ϵ using two independent instruments near the wavy sea surface.*
2. *provide the required data analysis techniques and assumptions in the presence of wave forcing.*

3. *modify GOTM by including both wave breaking and LC effects.*
4. *use the proposed scaling of ε for breaking and non-breaking waves, and wave-turbulence interaction, and perform comparisons with observed ε .*

In this paper, measurements of upper ocean turbulence are carried out using shear probes mounted on a free-falling profiler (MSS) and MATS. The GOTM model was modified this time to include wave breaking and LC effects using theory developed by Kantha and Clayson (2004). The numerical values of the TKE dissipation from the modified GOTM k - ε model are compared with the observed values of ε from MATS and MSS.

Paper V. The influence of surface gravity waves on the injection of turbulence in the upper ocean

1. *address a new data set for ε based on MATS shear probe signals, covering two storm periods.*
2. *present processing methodology for motion-correction applied to raw data of pressure, in order to estimate the one-dimensional wave energy frequency spectrum at the sea surface.*
3. *test the accuracy of the wave-modified GOTM model results with respect to the observed values of ε .*
4. *compare various methods of scaling ε with the values measured by MATS shear probes.*

Observations were made in the near-surface layer, at approximately 8 m below the sea surface for a duration of 2.5 months in late 2011, covering two storm periods. The time series of ε measured from MATS shear probes and the estimates of surface gravity waves from the high-resolution pressure sensor are analysed here in more detail than in **Paper IV**. The passage of two low pressure systems with strong wind and wave forcing has provided an excellent opportunity to study upper ocean turbulence variability under severe conditions. Numerical calculations were performed using a second-order turbulence closure scheme based on the Mellor-Yamada level 2.5 scheme, modified to incorporate near-surface processes such as Langmuir circulations and wave breaking with slight changes in the representation of wave breaking than those used in **Paper IV**.

Paper VI. Wave-induced characteristics of atmospheric turbulence flux measurements

1. *decontaminate the wind velocity data measured using a sonic anemometer located approximately 3.7 m above the sea surface, in order to remove wave-induced platform motion disturbances.*
2. *compare corrected measurements obtained from the buoy-mounted DCF system (moving platform) with the ASIT data (fixed platform).*

3. *investigate the relation between measured fluxes and wave-induced momentum flux in the wave-affected marine boundary layer.*

In this paper, we focus on estimates of momentum flux obtained using the eddy correlation method applied to the data measured from a moored buoy deployed near a research Air-Sea Interaction Tower (ASIT) at Martha's Vineyard Coastal Observatory, Massachusetts, during spring 2010. The accuracy of the motion correction algorithms are checked by comparing their results with the corresponding calculated fluxes from ASIT. Numerical model estimates of momentum flux were also obtained using a wave model to calculate a sea-state dependent drag coefficient.

Chapter 6

Conclusions and general perspectives

6.1 Main results

As the presentation of papers in the previous chapter suggests, this thesis aims to address the impact of surface gravity waves on the near sea surface turbulence structure, both numerically and observationally. Overall, the findings of this study support the view that the turbulence below surface gravity waves does not obey the law of the wall.

The principle conclusions of this study can be summarized as:

1. A Microstructure Autonomous ocean Turbulence System (MATS) has been developed, offering a sophisticated way to obtain long time series of turbulence in the upper ocean boundary layer. This instrument is able to measure simultaneously both current speed, pressure, and the rate of dissipation of Turbulent Kinetic Energy (TKE) at a fixed depth below the sea surface. It is thus now possible to collect data sets which are large enough for adequate statistical analysis.
2. The use of a high resolution pressure transducer to measure sea surface elevation has permitted higher quality estimates of turbulent fluxes from floating platforms, especially during harsh weather conditions when other types of floating platforms cannot operate efficiently.
3. A collection of signal processing tools has been developed and implemented, which calculates various required manipulations and transformations performed on a measured signal contaminated by motions of the carrier platform, wave-induced disturbances, and mechanical vibrations of the platform.
4. The deployment of this moored moving platform during two storm periods has provided a good opportunity for the collection, analysis, and interpretation of the data describing physical processes near the sea surface. Such measurements are difficult to make from any other platform in harsh weather conditions.
5. A one-dimensional vertical mixing model has been modified to incorporate the influence of surface gravity waves. The skills of the modifications have been evaluated by conducting a series of ideal numerical experiments and model-observation inter-comparison scenarios.

6. The vertical structure of the TKE dissipation rate has been empirically parameterized by the use of some simplified formulations that include the effects of breaking and non-breaking waves, shear production, and Langmuir circulations.

6.2 Proposed future work

Although the results presented here have demonstrated the effectiveness of the MATS in measuring near surface oceanic turbulence parameters, this system needs to be further developed in a number of ways:

1. Investigate the probable reason for the high noise level in the measurements of the velocity field from the ADV mounted on the MATS, and try to develop the necessary processing techniques to remove such disturbances from the original signals.
2. Estimate the dissipation rates of TKE from thermistor measurements near the sea surface in the presence of wave forcing.
3. Estimate the directional wave energy spectrum using combined ADV and pressure signals.
4. Study of the wave effects on platform motion to develop further the results for the offshore platforms dynamics under interaction with surface gravity waves.
5. Modify and improve MATS in order to measure turbulent fluxes more accurately very close to the sea surface during wave breaking events in particular.

Although surface gravity waves are a probable major contributor to the enhancement of TKE near the sea surface, the effects of buoyancy and internal waves on the energetics of small-scale turbulent eddies and their interaction with surface gravity waves should be explored, due to the large variations in thermal stability which are observed in the upper ocean boundary layer. Furthermore, the present investigation provides a substantial basis to study how closely the Large Eddy Simulation model results can replicate the prediction of our wave-modified vertical ocean mixing model results. This challenging investigation, together with the collection and analysis of accurate data sets near the wavy sea surface would be the subject of many future studies.

The coupling methodologies together with wave-modified closure (the algebraic Reynolds stress) models can be extended further to the regional models. In addition, terms such as pressure-correlation need to be more explored for deriving the efficient stability functions when wave effects are included in the model simulation runs.

References

- Agrawal, Y. C., E. A. Terray, M. A. Donelan, P. A. Hwang, A. J. Williams-III, W. M. Drennan, K. K. Kahma, and S. A. Kitaigorodskii, 1992: Enhanced dissipation of kinetic energy beneath surface waves. *Nature*, **359**, 219–220. 3.3
- Aiki, H. and R. Greatbatch, 2012: Thickness-weighted mean theory for the effect of surface gravity waves on mean flows in the upper ocean. *J. Phys. Oceanogr.*, **42**, 725–747. 3, 2.2.3, 2.2.3
- Andrews, D. and M. McIntyre, 1978: An exact theory of nonlinear waves on a Lagrangian mean flow. *J. Fluid Mech.*, **89**, 609–646. 2.2.3
- Anis, A. and J. N. Moum, 1995: Surface wave-turbulence interactions: Scaling $\varepsilon(z)$ near the sea surface. *J. Phys. Oceanogr.*, **25**, 2025–2045. 2.3, 2.3.1, 3.3
- Ardhuin, F. and T. Elfouhaily, 2004: Waves and the air-sea momentum budget: Implications for ocean circulation modeling. *J. Phys. Oceanogr.*, **34**, 1741–1755. 2.2.2
- Ardhuin, F. and A. D. Jenkins, 2006: On the interaction of surface wave and upper ocean turbulence. *J. Phys. Oceanogr.*, **36**, 551–557. 1
- Ardhuin, F., N. Raschle, and K. B. Belibassakis, 2008: Explicit wave-averaged primitive equations using a generalized lagrangian mean. *Ocean Mode*, **20**, 35–60. 3, 2.2.3
- Babanin, A. V. and B. K. Haus, 2009: On the existence of water turbulence induced by nonbreaking surface waves. *J. Phys. Oceanogr.*, **39**, 2675–2679. 1, 2.3
- Bakhoday-Paskyabi, M. and I. Fer, 2014a: The influence of surface gravity waves on the injection of turbulence in the upper ocean. *Nonlin. Proc. Geophys.* accepted for publication. 1
- Bakhoday-Paskyabi, M. and I. Fer, 2014b: Turbulence structure in the upper ocean: a comparative study of observations and modelling. *Ocean Dyn.* DOI 10.1007/s10236-014-0697-6. 1
- Bakhoday-Paskyabi, M., I. Fer, and A. D. Jenkins, 2012: Surface gravity wave effects on the upper ocean boundary layer: Modification of a one-dimensional vertical mixing model. *Cont. Shelf Res.*, **38**, 63–78. 1
- Belcher, S. E., A. L. M. Grant, K. E. Hanley, B. Fox-Kemper, L. V. Roedel, P. P. Sullivan, W. G. Large, A. Brown, A. Hines, D. Calvert, A. Rutgersson, H. Pettersson, J.-R. Bidlot, P. A. E. M. Janssen, and J. A. Polton, 2012: A global perspective on

- Langmuir turbulence in the ocean surface boundary layer. *Geophys. Res. Lett.*, **39**, doi:10.1029/2012GL052932. 1, 1.1, 1.3, 1, 2.3.3, 2.3.3
- Benilov, A. Y. and L. N. Ly, 2002: Modelling of surface wave breaking effects in the ocean upper layer. *Math. and Comp. Modelling*, **35**, 191–213. 1
- Broström, G., K. H. Christensen, and J. E. H. Weber, 2008: A quasi-Eulerian, quasi-Lagrangian view of surface-wave-induced flow in the ocean. *J. Phys. Oceanogr.*, **38**, 1122–1130. 2.2.2
- Burchard, H., 2001: Simulating the wave-enhanced layer under breaking surface waves with two-equation turbulence models. *J. Phys. Oceanogr.*, **31**, 3133–3145. 1, 2.3, 3.1, 3.1
- Cheung, T. K. and R. L. Street, 1988: Turbulent layers in the water at an air-water interface. *J. Fluid Mech.*, **194**, 133–151. 2.3, 3.3
- Churchill, J. and G. Csanady, 1983: Near-surface measurements of quasi-Lagrangian velocities in open water. *J. Phy. Oceanogr.*, **13**, 1669–1680. 3.3
- Craig, P. D., 1996: Velocity profiles and surface roughness under breaking waves. *J. Geophys. Res.*, **101(C1)**, 1265–1277. 1, 2.3, 3.1, 3.1
- Craig, P. D. and M. L. Banner, 1994: Modeling wave-enhanced turbulence in the ocean surface layer. *J. Phys. Oceanogr.*, **24**, 2546–2559. 1, 2.3, 3.1, 3.1
- Craik, A. D. D. and S. Leibovich, 1976: A rational model for Langmuir circulations. *J. Fluid Mech.*, **73**, 401–426. 1, 1, 2.2.1, 2.2.1
- Dai, D., F. Qiao, W. Sulisz, L. Han, and A. V. Babanin, 2010: Notes and correspondence: An experiment on the nonbreaking surface-wave-induced vertical mixing. *J. Phys. Oceanogr.*, **40**, 2180–2188. 1
- D’Alessio, S. J. D., K. Abdella, and N. A. McFarlane, 1998: A new second-order turbulence closure scheme for modeling the oceanic mixed layer. *J. Phys. Oceanogr.*, **28**, 1624–1641. 3.1
- D’Asaro, E. A., J. Thomson, A. Y. Scherbina, R. R. Harcourt, M. F. Cronin, M. A. Hemer, and B. Fox-Kemper, 2014: Quantifying upper ocean turbulence driven by surface waves. *Geophys. Res. Lett.*, **42**, 1–6, doi:10.1002/2013GL058193. 1
- Duncan, J., 1981: An experimental investigation of breaking waves produced by a towed hydrofoil. *Proc. Roy. Soc. London*, **A377**, 331–348. 3.1
- Dupuis, H., C. Gurin, D. Hauser, A. Weill, P. Nacass, W. Drennan, S. Cloch, and H. Graber, 2003: Impact of flow distortion corrections on turbulent fluxes estimated by the inertial dissipation method during the FETCH experiment on R/V L’Atalante. *J. Geophys. Res.*, **108 (C3)**, 8064, doi:10.1029/2001JC001075. 4.2.1
- Edson, J. B., A. A. Hinton, K. E. Prada, J. E. Hare, and C. W. Fairall, 1998: Direct covariance flux estimates from mobile platforms at sea. *J. Atmos. Oceanic Technol.*, **15**, 547–562. 3.3, 4.2.1

- Fer, I. and M. Bakhoday-Paskyabi, 2014: Autonomous ocean turbulence measurements with a moored instrument. *J. Atmos. Ocean. Tech.*, **31**, 474–490. 2.3
- Fujitani, T., 1981: Direct measurement of turbulent fluxes over the sea during AMTEX. *J. Meteor. Geophys.*, **32**, 119–134. 3.3
- Garrett, C., 1976: Generation of Langmuir circulations by surface waves: A feedback mechanism. *J. Mar. Res.*, **34**, 116–130. 1
- Gemmrich, J., 2010: Strong turbulence in the wave crest region. *J. Phys. Oceanogr.*, **40(3)**, 583–595. 3.1
- Gemmrich, J. and D. M. Farmer, 1999: Near-surface turbulence and thermal structure in a wind-driven sea. *J. Phys. Oceanogr.*, **29**, 480–499. 3.1, 3.1
- Gemmrich, J. R. and D. M. Farmer, 2004: Near-surface turbulence in the presence of breaking waves. *J. Phys. Oceanogr.*, **34**, 1068–1086. 1, 2.3, 3.1
- Gerbi, G. P., J. H. Trowbridge, E. A. Terray, A. J. Plueddemann, and T. Kukulka, 2009: Observations of turbulence in the ocean surface boundary layer: Energetics and transport. *J. Phys. Oceanogr.*, **39**, 1077–1096. 3.1
- Goodman, L., E. R. Levine, and R. G. Lueck, 2006: On measuring the terms of the turbulent kinetic energy budget from an AUV. *J. Atmos. Ocean. Technol.*, **23**, 977–990. 4.2.1
- Haas, K. A., I. A. Svendsen, M. C. Haller, and Q. Zhao, 2003: Quasi-three-dimensional modeling of rip current systems. *J. Geophys. Res.*, **108**. 2.2.2
- Harcourt, R. R., 2013: A second moment closure model of Langmuir turbulence. *J. Phys. Oceanogr.*, **43**, 673–697. 2.3.2, 2.3.2, 2.3.2, 2.3.2, 3.1
- Hasselmann, K., 1970: Wave-driven inertial oscillations. *Geophys. Fluid Dyn.*, **1**, 463–502. 1
- Huang, C. J., F. Qiao, Z. Song, and T. Ezer, 2011: Improving simulation of the upper ocean by inclusion of surface waves in the Mellor-Yamada turbulence scheme. *J. Geophys. Res.*, **116**. 3.1
- Huang, N. E., 1971: Derivation of Stokes drift for a deep-water random gravity wave field. *Deep Sea Res.*, **18**, 255–259. 1
- Janssen, P. A. E. M., 2012: Ocean wave effects on the daily cycle in SST. *J. Geophys. Res.*, **117**, 1–24. 3.1
- Jenkins, A. D., 1986: A theory for steady and variable wind and wave induced currents. *J. Phys. Oceanogr.*, **16**, 1370–1377. 1, 1, 3
- Jenkins, A. D., 1987: Wind and wave induced currents in a rotating sea with depth-varying eddy viscosity. *J. Phys. Oceanogr.*, **17**, 938–951. 1, 1, 3, 5
- Jenkins, A. D., 1989: The use of a wave prediction model for driving a near-surface current model. *Dtsch. Hydrogr. Z.*, **42**, 133–149. 1, 3, 5

- Jenkins, A. D., M. Bakhoday-Paskyabi, I. Fer, A. Gupta, and M. Adakudlu, 2012: Modelling the effect of ocean waves on the atmospheric and ocean boundary layers. *Energ. Proc.*, **24**, 166–175. 3.1
- Jiang, J. S. and R. L. Street, 1991: Modulated flows beneath wind-ruffled, mechanically generated water waves. *J. Geophys. Res.*, **96**, 2711–2721. 2, 2.3, 2.3.1
- Jones, L. S. F., 1985: Turbulence below wind waves. *The Ocean Surface (ed. Y. Toba & H. Mitsuyasu)*. Reidel, 437–442. 3.3
- Jones, N. L. and S. G. Monismith, 2007: The influence of whitecapping waves on the vertical structure of turbulence in a shallow estuarine embayment. *J. Phys. Oceanogr.*, **38**, 1563–1580. 3.1
- Kantha, L. and C. Clayson, 1994: An improved mixed layer model for geophysical applications. *J. Geophys. Res.*, **99**, 25235–25266. 2.3.2
- Kantha, L. H. and C. A. Clayson, 2004: On the effect of surface gravity waves on mixing in the oceanic mixed layer. *Ocean Modelling*, **6**(2), 101–124. 3.1, 3.1, 5
- Kitaigorodskii, S. A., M. A. Donelan, J. L. Lumley, and E. A. Terray, 1983: Wave-turbulence interactions in the upper ocean. Part II: statistical characteristics of wave and turbulent components of the random velocity field in the marine surface layer. *J. Phys. Oceanogr.*, **13**, 1988–1999. 2.3, 2.3.1, 3.3
- Kitaigorodskii, S. A. and J. L. Lumley, 1983: Wave-turbulence interactions in the upper ocean. Part I: The energy balance of the interacting fields of surface wind waves and wind-induced three-dimensional turbulence. *J. Phys. Oceanogr.*, **13**, 1977–1987. 1, 2.3, 2.3.1, 3.3
- Kudryavtsev, V., V. Shrira, V. Dulov, and V. Malinovsky, 2008: On the vertical structure of wind-driven sea currents. *J. Phys. Oceanogr.*, **38** (10), 2121–2144. 1
- Kudryavtsev, V. N. and V. K. Makin, 2001: The impact of air-flow separation on the drag of the sea surface. *Bound. Layer Meteor.*, **98**, 155–171. 2.1
- Kudryavtsev, V. N. and V. K. Makin, 2002: Coupled dynamics of short waves and the airflow over long surface waves. *J. Geophys. Res.*, **107**(C12). 2.1
- Lamarre, E. and W. K. Melville, 1991: Air entrainment and dissipation in breaking waves. *Nature*, **351**, 469–472. 1
- Lamb, H., 1932: *Hydrodynamics*. Cambridge [Eng.]: University Press. 4.2.1, 4.2.1
- Lane, E., J. M. Restrepo, and J. C. McWilliams, 2007: Wave-current interaction: A comparison of radiation-stress and vortex-force representations. *J. Phys. Oceanogr.*, **37**, 1122–1141. 2.2.1, 2.2.2
- Leibovich, S., 1983: The form and dynamics of Langmuir circulations. *Annu. Rev. Fluid Mech.*, **15**, 391–427. 1

- Loewen, M. and W. Melville, 1991: Microwave backscatter and acoustic radiation from breaking waves. *J. Fluid Mech.*, **224**, 601–623. 3.1
- Longuet-Higgins, M. S., 1953: Mass transport in water waves. *Philos. Trans. R. Soc., Ser. A*, **245**, 535–581. 1
- Longuet-Higgins, M. S. and R. W. Stewart, 1962: Radiation stress and mass transport in gravity waves, with application to surf-beats. *J. Fluid Mech.*, **13**, 481–562. 2, 2.2.2, 2.2.2
- Longuet-Higgins, M. S. and R. W. Stewart, 1964: Radiation stresses in water waves; a physical discussion, with applications. *Deep-Sea Res.*, **11**, 529–562. 2, 2.2.2, 2.2.2
- Lumley, J. L. and E. A. Terray, 1983: Kinematics of turbulence convected by a random wave field. *J. Phys. Oceanogr.*, **13**, 2000–2007. 2.3, 3.3
- Magnaudet, J. and L. Thais, 1995: Orbital rotational motion and turbulence below laboratory wind water waves. *J. Geophys. Res.*, **100**, 757–771. 2.3
- McWilliams, J. C., E. Huckle, J. H. Liang, and P. P. Sullivan, 2012a: The wavy Ekman layer: Langmuir circulations, breaking waves, and Reynolds stress. *J. Phys. Oceanogr.*, **42**, 1793–1816. 1
- McWilliams, J. C., E. Huckle, J. H. Liang, and P. P. Sullivan, 2012b: The wavy Ekman layer: Langmuir circulations, breaking waves, and Reynolds stress. *J. Phys. Oceanogr.*, **42**, 1793–1816. 2.3.2
- McWilliams, J. C. and E. M. Lane, 2004: An asymptotic theory for the interaction of waves and currents in coastal waters. *J. Fluid Mech.*, **511**, 135–178. 2.2.1
- McWilliams, J. C. and J. M. Restrepo, 1999: The wave-driven ocean circulation. *J. Phys. Oceanogr.*, **29**, 2523–2540. 1, 2.2.1, 2.2.1
- McWilliams, J. C., P. P. Sullivan, and C. H. Moeng, 1997: Langmuir turbulence in the ocean. *J. Fluid Mech.*, **334**, 1–30. 3.1
- Mellor, G., 2003: The three-dimensional current and surface wave equations. *J. Phys. Oceanogr.*, **33**, 1978–1989. 3, 2.2.2, 2.2.3
- Mellor, G., 2013: Pressure–slope momentum transfer in ocean surface boundary layers coupled with gravity waves. *J. Phys. Oceanogr.*, **43**, 2173–2184. 1, 3.1
- Mellor, G., M. A. Donelan, and L. Y. Oey, 2008: A surface wave model for coupling with numerical ocean circulation models. *J. Atmos. Oceanic Technol.*, **35**, 1785–1807. 2.2.2, 2.2.3
- Mellor, G. L. and T. Yamada, 1982: Development of a turbulence closure model for geophysical fluid problems. *Rev. Geophys. Space Phys.*, **20**, 851–875. 1, 2.3.2
- Melsom, A., 1996: Effects of wave breaking on the surface drift. *J. Geophys. Res.*, **101**, 12071–12078, doi:10.1029/96JC00584. 1

- Melville, W. and P. Matusov, 2002: Distribution of breaking waves at the ocean surface. *Nature*, **417**, 58–63. 1, 1, 3.1
- Noh, Y., H. S. Min, and S. Raasch, 2004: Large eddy simulation of the ocean mixed layer: The effects of wave breaking and langmuir circulation. *J. Phys. Oceanogr.*, **34**, 720–735. 3.1
- Oost, W., C. Fairall, J. Edson, S.D.Smith, R. Anderson, J. Willis, K. Katsaros, and J. DeCosmo, 1994: Flow distortion calculations and their application in HEXMAX. *J. Atmos. Ocean. Tech.*, **11**, 366–381. 4.2.1
- Osborn, T. R., D. M. Farmer, S. Vagle, S. A. Thorpe, and M. Cure, 1992: Measurements of bubble plumes and turbulence from a submarine. *Atmos. Ocean*, **30**, 419–440. 3.3
- Pedrerros, R., G. Dardier, H. Dupuis, H. Graber, W. Drennan, A. Weill, C. Gurin, and P. Nacass, 2003: Momentum and heat fluxes via the eddy correlation method on the R/V L'Atalante and an ASIS buoy. *J. of Geophy. Res.*, **108**, (C11), 3339, doi:10.1029/2002JC001449. 3.3
- Phillips, M., 1985: Spectral and statistical properties of the equilibrium range in wind-generated gravity waves. *J. Fluid Mech.*, **156**, 495–531. 3.1
- Pollard, R., 1973: Interpretation of near-surface current meter observations. *Deep-Sea Res.*, **20**(3), 261–268. 1
- Qiao, F., Y. Yuan, Y. Yang, Q. Zheng, C. Xia, and J. Ma, 2004: Wave-induced mixing in the upper ocean: Distribution and application to global ocean circulation model. *Geophys. Res. Lett.*, **31**, L11303, doi:10.1029/2004GL019824. 1
- Rapp, R. J. and W. K. Melville, 1990: Laboratory measurements of deep-water breaking waves. *Philosophical Transactions of the Royal Society of London A*, **331**, 735–800. 1, 1, 2.3, 3.1
- Raschle, N., F. Ardhuin, and E. A. Terray, 2007: Drift and mixing under the ocean surface: A coherent one-dimensional description with application to unstratified conditions. *J. Geophys. Res.*, **111**, C03016, doi:10.1029/2005JC003004. 3.1
- Raschle, N., B. Chapron, F. Ardhuin, and A. Soloviev, 2012: A note on the direct injection of turbulence by breaking waves. *Ocean Model.* 1–7, doi:10.1016/j.ocemod.2012.09.001. 1, 3.1
- Restrepo, J. M., 2007: Wave breaking dissipation in the wave-driven ocean circulation. *J. Phys. Oceanogr.*, **37**, 1749–1763. 2.2.1
- Smith, J. A., 2006: Wave-current interactions in finite depth. *J. Phys. Oceanogr.*, **36**, 1403–1419. 2.2.2, 2.2.2
- Soloviev, A., R. Lukas, P. Hacker, H. S. M. Baker, and A. Arjannikov, 1998: A near-surface microstructure sensor system used during TOGA COARE. Part II: Turbulence measurements. *J. Atmos. Oceanic Technol.*, **16**, 1598–1618. 1

- Stips, A., H. Burchard, K. Bolding, H. Prandke, A. Simon, and A. Wüest, 2005: Measurement and simulation of viscous dissipation in the wave affected surface layer. *Deep Sea Res. II*, **52**, 1133–1155. 3.1
- Sullivan, P. P., J. C. McWilliams, and W. K. Melville, 2004: The oceanic boundary layer driven by wave breaking with stochastic variability. Part i. direct numerical simulations. *J. Fluid Mech.*, **507**, 143–174. 1, 1, 1, 3.1
- Sullivan, P. P., J. C. McWilliams, and W. K. Melville, 2007: Surface gravity wave effects in the oceanic boundary layer: large-eddy simulation with vortex force and stochastic breakers. *J. Fluid Mech.*, **593**, 405–452. 1, 1, 3.1
- Sullivan, P. P., L. Romero, J. C. McWilliams, and W. K. Melville, 2012: Transient evolution of Langmuir turbulence in the ocean boundary layers driven by hurricane winds and waves. *J. Phys. Oceanogr.*, **42**, 1959–1979. 3.1
- Sutherland, G., B. Ward, and K. H. Christensen, 2013: Wave-turbulence scaling in the ocean mixed layer. *Ocean Sci.*, **9**, 597–608. 3.3
- Tang, C. L., W. Perrie, A. D. Jenkins, B. M. DecTracy, and T. B., 2007: Observation and modeling of surface currents on the Grand Banks: A study of the wave effects on surface currents. *J. Geophys. Res.*, **112**, 1–16. 1
- Taylor, G., 1935: Statistical theory of turbulence. *Proceedings of the Royal Society of London. Series A, Mathematical and Physical Sciences*, **151(873)**, 421–444. 4.2.1
- Teixeira, M. A. C. and S. Belcher, 2002: On the distortion of turbulence by a progressive surface wave. *J. Fluid Mech.*, **458**, 229–267. 1, 2.3
- Tejada-Martinez, A. E., C. E. Grosch, N. Sinha, C. Akan, and G. Martinat, 2012: Disruption of the bottom log layer in large-eddy simulations of full-depth Langmuir circulation. *J. Fluid Mech.*, **699**, 79–93. 3.1, 3.1
- Terray, E. A. and L. F. Bliven, 1985: The vertical structure of turbulence beneath gently breaking waves. In *The Ocean Surface (ed. Y. Toba & H. Mitsuyasu)*. Reidel. 2.3
- Terray, E. A., M. A. Donelan, Y. C. Agrawal, W. M. Drennan, K. K. Kahma, A. J. Williams, P. A. Hwang, and S. A. Kitaigorodski, 1996: Estimates of kinetic energy dissipation under breaking waves. *J. Phys. Oceanogr.*, **26**, 792–807. 1, 3.1, 3.1
- Thais, L. and J. Magnaudet, 1996: Turbulent structure beneath surface gravity waves sheared by the wind. *J. Fluid Mech.*, **328**, 313–344. 2.3, 2.3.1
- Thompson, S. and J. Turner, 1975: Mixing across an interface due to grid turbulence generated by an oscillating grid. *J. Fluid Mech.*, **67(2)**, 349–368. 3.3
- Thorpe, S. A. and A. Hall, 1983: The characteristics of breaking waves, bubble clouds and near-surface currents observed using side-scan sonar. *Cont. Shelf Res.*, **1**, 353–384. 3.3
- Thorpe, S. A. and P. Humphries, 1980: Bubbles and breaking waves. *Nature*, **283**, 463–465. 1, 3.3

- Tian, Z., M. Perlin, and W. Choi, 2010: Energy dissipation in two-dimensional unsteady plunging breakers and an eddy viscosity model. *J. Fluid Mech.*, **655**, 217–257. 3.1
- Ursell, F., 1950: On the theoretical form of ocean swell on a rotating earth. *Mon. Not. R. Astron. Soc.*, **6**, 1–8. 1
- Weber, J. E., 1983a: Attenuated wave-induced drift in a viscous rotating ocean. *J. Fluid Mech.*, **137**, 115–129. 1, 3
- Weber, J. E., 1983b: Steady wind and wave induced currents in the open ocean. *J. Phys. Oceanogr.*, **13**, 524–530. 1, 3
- Weir, B., 2010: *The transfer of momentum from waves to currents due to wave breaking*. PhD thesis, The University of Arizona. 1, 2.2.1
- Xia, H., Z. Xia, and L. Zhu, 2004: Vertical variation in radiation stress and wave-induced current. *Coastal Engineer.*, **51**, 309–321. 2.2.2